Exclusive Meson Electroproduction

Georgie Mbianda Njencheu

A dissertation submitted to the Faculty of Science,
University of the Witwatersrand, Johannesburg,
in fulfillment of the requirments for the
degree of Masters of Science.

Johannesburg, 2008

Candidate's Declaration

I declare that this thesis is my own, unaided work. It is being submitted for the degree of Masters of Science in the University of the Witwatersrand, Johannesburg. It has not been submitted before for any degree or examination at any other University.

_____

Georgie Mbianda Njencheu (candidate)

_____ day of _____ 2008

Abstract

Jefferson Lab experiment E01-002 obtained data that can be used to determine the cross section of the process $p(e, e'\pi^+)n$ at the invariant mass range of 1.3 GeV $\leq W \leq 2.0$ GeV (second and third resonance regions) and at a forward angular range of $0.6 \leq \cos\theta_{cm} \leq 1$. These data have recently been used for resonance studies that have employed the π^0 and η channels to study the lower mass states like $\Delta(1232)$ and the $S_{11}(1535)$. However, many of the higher mass isospin $\frac{1}{2}$ resonances couple more strongly to the $\pi^+ n$ channel. With data from E01-002, this dissertation presents the cross section obtained on this channel at an average Q^2 value of 5.5 GeV^2. This is the highest Q^2 measurement of this exclusive process to date. The results are sensitive to high-mass resonances and diverge significantly from a recent theoretical model extrapolation of lower Q^2 data.

Acknowledgements

It will be difficult to thank everyone who contributed to this achievement. However I will attempt to mention everyone that I can.

I wish to thank my supervisors, Simon Connell and Peter Bosted for giving me the opportunity to work on this experiment. I am grateful for their help, support and guidance. They have been very generous and are truly respectful persons. Simon is a dynamic physicist and has the prime interest of promoting physics research in Africa, I wish to emulate him.

My special thanks goes to Mark Dalton from whom I benefited enormously from his accessibility and willingness to discuss any issue I encountered, ranging from the usage of the ROOT Analysis Frame Work to the adaptation of his analysis engine to suit my experiment. I can't speculate on the level of analysis I would have attained without Mark's huge assistance.

Of course I have to thank the rest of the JLab (Hall C) Baryon Collaboration members, most especially, Mark Jones who assisted me a lot with computing at JLab, Paul Stoler and Anthony Villano for each contributing in many more ways than one to the progress of this work.

Joining the Particle Solid Interaction (PSI) group has introduced me to fantastic people who have helped me in innumerable ways. I must thank Claire Lee, Attah Doom-Null Unwuchola, Marothi Phoku, Welleminah Mampe, Morgan Madhuku, Winile Sibande and specifically Sergio Ballestrero, who together with Simon, introduced me to the assembling and calibration of detectors, and the use of detectors in the acquisition of data.

I have had the privilege to have been taught by Robert de Mello Koch at the African Institute for Mathematical Sciences (AIMS), through whom I was introduced to Simon and hence to this project. At the final stage of this work, Robert helped as a 'nominal' supervisor for me to obtain NRF funding for the 2008 academic year via Wits university. Many thanks to Robert.

This work is supported in part by research grants from the U.S. Department of Energy, the U.S. National Science Foundation, the South African National Research Foundation and the African Institute for Mathematical Sciences.

Contents

List of Figures

List of Tables

Chapter 1

Introduction

This dissertation describes the measurement of the differential cross section for the process $p(e, e'\pi^+)n$ which is an adaptation from experiment E01-002 (Baryon Resonance Electroproduction at high Momentum Transfer) performed in Hall C of the Thomas Jefferson National Accelerator Facility from 29 April until 18 June 2003.

1.1 Fundamental Particles

The fundamental nature of matter in terms of elementary particles and their interactions is the central topic in subatomic physics. From the nuclear physics perspective, the atom consists of a cloud of electrons surrounding a positively charged nucleus, which contains protons and neutrons. The protons and neutrons, collectively called nucleons, are held together by the strong nuclear force via the exchange of mesons, for example, pions. Hadrons, i.e., strongly interacting particles like nucleons or pions, are not

elementary particles themselves but instead exhibit a substructure based on more fundamental particles, the so-called partons (in a particular model). The electrons, on the other hand, are believed to be fundamental in nature.

Studying the structure of the nucleon (a form of hadronic matter) and its excited states has been one of the most extensively investigated subjects in nuclear and particle physics for many years, because it allows us to understand important aspects of the underlying theory of the 'strong force'. One can study the ground state nucleon using elastic scattering of electrons off protons and neutrons while the excited state can only be studied via the transitions from the ground states into the nucleon resonances. This is because the excited states lifetimes are too short to make a target of excited nucleon technically feasible.

Electron scattering has been a very powerful tool for studying nucleon structure. This technique was used to discover the first evidence of proton substructure [2] and later to firmly establish the existence of the partons [3]. It is now being used to study the details of how elementary fields (quarks and gluons) form the experimentally observed baryons and mesons.

The excited states of the nucleon are unstable, rapidly decaying into meson-nucleon states. Due to the small mass of the pion, the single pion-nucleon decay is the favorite channel for many resonances, and not surprisingly, single pion electroproduction is being extensively exploited to under-

stand the structure of nucleon.

1.2 The Structure of the Dissertation

In this chapter we shall discuss the goal of the experiment and review the experimental formalism necessary to describe the measurement. We shall discuss the cross section for the pion electroproduction process and state how it is calculated.

Chapter 2 reviews the theory of quarks. We present various theoretical models of pion electroproduction giving a historical survey of the theoretical and experimental developments surrounding the study of spin $\frac{1}{2}$ resonances in general. An overview of existing experimental data for pion electroproduction is also discussed.

Chapter 3 explains the electron accelerator, cryogenic liquid hydrogen target, magnetic spectrometers, detectors, and other instrumentation used in the acquisition of data.

Chapter 4 describes the Monte Carlo simulation of the experiment. This simulation included multiple scattering, ionization energy losses, pion decay, and radiative processes.

Chapter 5 elaborates all steps taken during the analysis of the data. Here we explain how the data was corrected for pion absorption and radiative processes. We describe the technique used to identify particles and select

the events of interest as well as the reconstruction of the missing neutron mass. We explain the checks performed, and the cuts made on the data. We outline the steps used for extracting the differential cross section and give our estimates of systematic uncertainties. How we arrive at those estimates is also explained.

In chapter 6 we discuss the result of the analysis in comparison to theoretical models and a recent pion electroproduction data from CLAS (JLab), we also illustrate the ϕ-dependence of the measured differential cross section. The importance of this data, which is from an extended kinematic region from previous data, is highlighted. We indicate how the data could be used to measure the Q^2 dependence of the transition form factors into higher mass resonances.

Appendix A consists of Table A.1 that gives for each bin the differential cross section, the weighted average Q^2 of events $\langle Q^2_{bin} \rangle$, the average longitudinal polarization of the virtual photon $\langle \epsilon \rangle$, the radiative correction factor, and the statistical and systematic errors.

1.3 Goal of the Experiment

The inclusive electron scattering spectrum clearly indicates three resonance regions above the elastic peak [4], but it does not allow us to separate different resonances which make up the second and higher resonance peaks. Even

in the first resonance region there is a considerable non-resonant background under the dominant $\Delta(1232)$ peak. Therefore, exclusive measurements in the hadronic center-of-mass are necessary to separate the background from contributions from different overlapping resonances.

The goal of this experiment is to measure the differential cross sections which can reveal information about the relative strength of the many and overlapping high mass resonances for the process $p(e, e'\pi^+)n$ at the average Q^2 of 5.5 GeV^2. This could then enable the extraction of valuable information to understand better the structure of the isospin $\frac{1}{2}$ resonances for which the $\pi^+ n$ decay is preferred over the $\pi^0 p$ channel.

1.4 Kinematic Definitions

We use the metric

$$g_{\mu\nu} = \begin{pmatrix} 1 & 0 & 0 & 0 \\ 0 & -1 & 0 & 0 \\ 0 & 0 & -1 & 0 \\ 0 & 0 & 0 & -1 \end{pmatrix}$$

so that the square of the invariant mass associated with a particle with four-momentum $p = (E, \mathbf{p})$ is given by

$$m^2 = p.p = E^2 - |\mathbf{p}|^2 > 0.$$

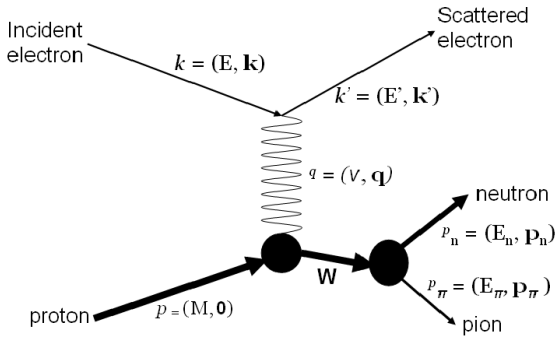

Figure 1.1: *The Born diagram of the resonance electroproduction process.*

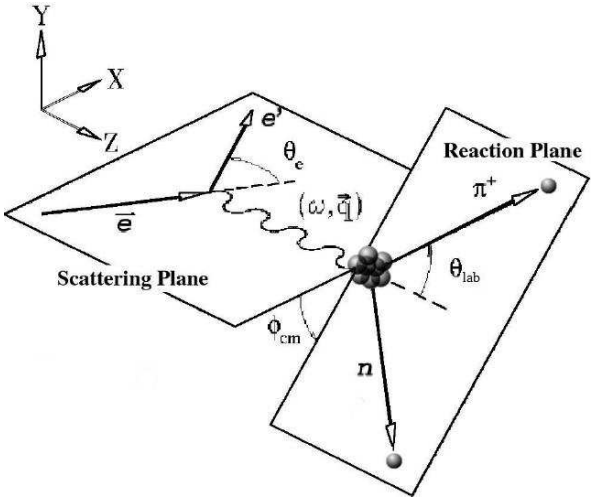

Figure 1.2: *Scattering and Reaction planes depicting θ_e and ϕ_{cm}. Figure adapted from Ref. [24].*

For this experiment, we are considering the interaction between an electron and a proton, see Figure 1.1. We define the following quantities:

- $k = (E, \mathbf{k})$, the four-momentum of the incident electron, with $|\mathbf{k}| \approx E$ (i.e., $m_e \approx 0$);
- $k' = (E', \mathbf{k}')$, the four-momentum of the outgoing electron, with $|\mathbf{k}'| \approx E'$;
- $p = (M, \mathbf{0})$, the four-momentum of the target proton (at rest in the lab frame);
- $p_\pi = (E_\pi, \mathbf{p}_\pi)$, the four-momentum of the outgoing pion;
- $q = (\nu, \mathbf{q})$, the four-momentum of the virtual photon, where $\nu = E - E'$ is the energy transferred.

With the above definitions and approximations we find that the mass-squared of the virtual photon is

$$q^2 = \nu^2 - |\mathbf{q}|^2 = -4EE' \sin^2(\theta_e/2) < 0.$$

A quantity more commonly used is $Q^2 \equiv -q^2 > 0$. In a similar fashion the square of the mass of the resonant state is

$$W^2 = s = (q + p)^2 = -Q^2 + M^2 + 2M\nu,$$

and the square of the four-momentum transferred to the nucleon is

$$t = (q - p_\pi)^2.$$

s and t are called *Mandelstam* variables. There are three in total, with the third being

$$u = (q - p_n)^2.$$

These are used in nuclear physics to describe and study the structure of the scattering amplitude. An advantage of these variables is that they are relativistically invariant, and therefore have the same value in both the lab and centre-of-mass frames.

In this experiment we measured the energy of the outgoing pion and reconstructed the square of the mass of the missing neutron from the components of the pion and electron three-momenta:

- the energy of the outgoing pion

  $$E_\pi = (m_\pi^2 + p_x^{'2} + p_y^{'2} + p_z^{'2})^{1/2},$$

  where m_π is mass of pion and p'_x, p'_y, and p'_z are the components of the three-momentum $\mathbf{p}'$ of the pion;

- the mass of the missing particle(s), X, from the process $e + p \rightarrow e' + \pi^+ + X$,

  $$M_x^2 = M_n^2 = (E - E' + M - E_\pi)^2 - (k'_x + p'_x)^2 - (k'_y + p'_y)^2 - (-k'_z - p'_z + E)^2,$$

where k'_x, k'_y, and k'_z are components of the three-momentum $\mathbf{k}'$ of the scattered electron.

1.5 Pion Electroproduction Cross Section

Experimental results on scattering are usually quoted in the form of a "cross section". The cross section may be regarded as the effective area over which the incident particle and the target interact to produce the ejectile and the residue. In this experiment the definition is more complicated. The primary incident particle is the electron, which produces a secondary incident particle, the virtual photon. The photon then interacts with the nucleon, and the exit channel where a pion and a neutron are emitted is studied. This leads to two reaction vertices.

The differential cross section for single pion electroproduction in the one photon exchange approximation can be written as a contraction between the lepton tensor $L_{\mu\nu}$ and a hadron tensor $W_{\mu\nu}$ [5]:

$$\frac{d^6\sigma}{d\Omega_e dE' d\Omega_\pi dE_\pi} = |\mathbf{P}_\pi| E_\pi \frac{\alpha^2}{Q^4} \frac{E'}{E} L_{\mu\nu} W^{\mu\nu} \tag{1.1}$$

The lepton tensor, associated with the electromagnetic vertex, can be calculated exactly in QED. The explicit structure of the hadron tensor depends on the specific process under investigation. If the final state is discrete as in

the case of the reaction $p(e, e'\pi^+)n$, the cross section reduces to a five-fold differential form:

$$\frac{d^5\sigma}{dE'd\Omega_e d\Omega_\pi} = \Gamma \frac{d^2\sigma}{d\Omega_\pi} \tag{1.2}$$

On the right-hand side of Equation (1.2) the electron part of the cross section is contracted into a virtual photon flux, Γ (the number of photons hitting the target per unit area and per unit time).

We use the following convention

$$\Gamma = \frac{\alpha}{2\pi^2}\frac{E'}{E}\frac{W^2 - M^2}{2MQ^2}\frac{1}{1-\epsilon}$$

where $\epsilon = (1 + 2\tan^2(\theta/2)|\mathbf{q}|^2/Q^2)^{-1}$ describes the ratio of longitudinal and transverse polarization of the virtual photon, $\alpha = \frac{e^2}{2\pi} \approx \frac{1}{137}$ (setting $\hbar = c = 1$) is the fine-structure constant and $(W^2 - M^2)/2M$ is the equivalent real-photon energy. The real-photon energy is the laboratory energy a real photon would need to produce a system with invariant mass W.

The result of the contraction of the lepton tensor and the hadron tensor is decomposed into four structure functions corresponding to the polarization states of the virtual photon: a longitudinal (L), a transverse (T) and two interference terms (LT and TT). The two-fold differential cross section for the pion production in Equation (1.2) can be expressed in terms of the structure function as:

$$\frac{d^2\sigma}{d\Omega_\pi} = \sigma_T + \epsilon\sigma_L + \epsilon\sigma_{TT}\cos 2\phi + \sqrt{\frac{\epsilon(1+\epsilon)}{2}}\sigma_{LT}\cos\phi \qquad (1.3)$$

where the σ_X, shorthand for $d\sigma_X/d\Omega_\pi$, depend on Q^2, W and t.

The four structure functions can be separated if measurements are done at different values of ϵ and ϕ_{cm}, while Q^2, W and t are kept constant. The photon polarization ϵ can be varied by changing the electron energy and scattering angle (the so-called "Rosenbluth-" or L/T-separation). The angle ϕ_{cm}, which describes the orientation of the hadronic decay plane with respect to the scattering plane (see Figure 1.2), can be varied by measuring the pion left and right of the **q**-vector (for σ_{LT}), and additionally out of the scattering plane (for σ_{TT}). At $\theta_{cm} = 0$, that is if the pion is detected in the direction of the **q**-vector (parallel kinematics), the interference terms are zero, and only σ_L and σ_T are left over.

Chapter 2

Theoretical Review

Hadrons (baryons and mesons) are particles that feel the strong interaction. Pions, neutron, protons etc. join nuclei and atoms as one more manifestation of bound-state structures that exist in a world of quarks and leptons. The theoretical framework to translate these conceptual developments into quantitative calculational schemes are "gauge" theories. Quantum Electrodynamics (QED), which describes electromagnetic interactions of electrons and photons, is the simplest example of such a theory. Quantum Chromodynamics (QCD) is the appropriate theory for strong interactions of quarks and gluons while the unified electroweak model applies for the weak interactions of leptons.

2.1 Quarks and Colour

The search for the multiplicity in the meson and baryon spectra led to the concepts of quarks and $SU(3)$ flavour symmetry with the three flavours

up(u), down(d), and strange(s). The (u,d,s) quarks have spin $\frac{1}{2}$, and carry fractional electric charge ($\frac{2}{3}e$,$-\frac{1}{3}e$,$-\frac{1}{3}e$). The quark scheme naturally accommodates the observed separation of hadrons into baryons (three quark or three antiquark fermion states) and mesons (quark-antiquark bosonic states). The structureless quarks, rather than the nucleons, are the fundamental entities described by quantum field theory. This quark scheme appeared to violate the Pauli exclusion principle which is expected to apply to spin $\frac{1}{2}$ quarks as it does for electrons. Now the Δ^{++}-baryon (the π^+p resonance), for instance, is supposed to consist of three identical u quarks in the same state; it appears to be inconsistent with the Pauli principle. This dilemma was overcome by the "colour" quantum number for quarks and the introduction of the $SU(3)$ colour symmetry so that the Δ^{++} could be written as $u_r u_g u_b$, where the spin-space-flavour part of the resonance's wave function can be symmetric if the colour part is antisymmetric [6, 7]. An assertion is that all observed particle states are colour singlets or "white". Since quarks are coloured, they are hidden from our sight. But there are nevertheless a multitude of ways to infer experimentally their existence in hadrons.

In quantum field theory, where elementary particle physics naturally falls, all forces of nature are a result of particle exchange. Quarks interact by the exchange of a virtual bi-coloured gluon, that is, quarks interact strongly by switching colour. The colour "charge" endows quarks with a colour field

that makes a "strong" force dominate the electromagnetic repulsion thereby binding the same charge u quarks in Δ^{++} for example.

2.2 Models of Pion Electroproduction

There are many different models for describing the electroexcitation of resonances via pion production, some of which are:

- Quark models
- Isobar models
- Born term models

The basic feature of QCD-inspired quark models [8, 9, 10, 11, 12] is as mostly described in Section 2.1. Amongst the many models of hadron structure that have been developed, the Constituent Quark Model (CQM) which consists of a 'dressed' quark (a bare quark together with a gluonic cloud) of several hundred MeV [4] can be singled out due to its capacity to offer both qualitative and quantitative explanations of experimental data at low energies (low Q^2).

Different levels of excitation of the QCD-inspired quark system corresponds to different resonances. The Constituent Quark Model (CQM) [8], was already very successful in describing the masses of the low lying baryon states with the radial excitation numbers $N = 0$ and $N = 1$. Quark models de-

scribe the excitation of nucleon resonances as a transition from the ground state to an excited state.

The isobar models describe pion electroproduction in the resonance region by calculating the total amplitude as a coherent sum of many nucleon production diagrams and a non-resonant background. One of the first such models was developed by R.L. Walker [13] to analyze pion photoproduction data. Later a similar model was used to analyze electroproduction data [14]. One of the best isobar models that successfully describes charged and neutral pion electroproduction data is the MAID [15], a Unitary Isobar Model (UIM) developed at University of Mainz . It uses effective Lagrangian methods to calculate the Born background, including ω and ρ meson exchange processes. The background amplitudes are unitarized with a $(1+if_{l\pm}^{\pi N})$ factor, where $f_{l\pm}^{\pi N}$ are the pion-nucleon scattering amplitudes. Another isobar parameterization dail-in code is the SAID [16, 17, 18] that has also been used to develop tools for performing amplitude analyzes of the Δ excitation data and determining the resonance parameters. Both codes are based on the same on-shell relation. While MAID includes only one hadron channel, πN (or ηN), into this relation, SAID uses three channels: γN, πN, and $\pi\Delta$.

The one-photon-exchange approximation assumes a scattered electron emits a single virtual photon which couples to, in this case, a nucleonic

system. The amplitude for this process is described as a sum of Feynman amplitudes for all reaction mechanisms that contribute to the process $\gamma + p \rightarrow \pi^+ + n$. In pion electroproduction, the Born (single photon exchange) terms are the first order processes that contribute to the amplitude, Figure 2.1. The process of interest to us is the s-channel resonance production.

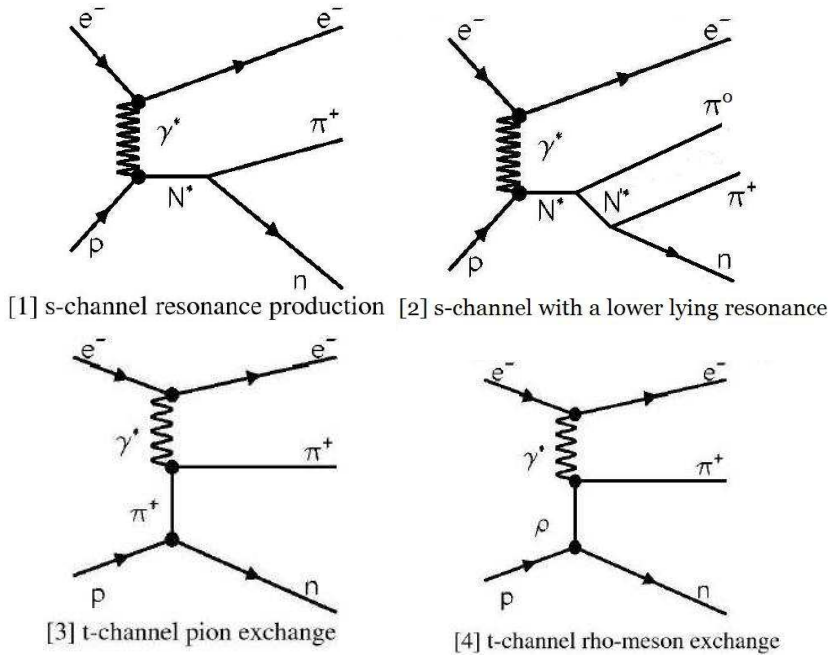

Figure 2.1: *Contributing Born terms of single π^+ electroproduction. Figure adapted from Ref. [24].*

Nucleon resonances

The study of transitions from the nucleon to high mass resonances can provide detailed information on the structure of the nucleon and its excited states. Particles at their excited states decay by strong interactions and do

not live long enough to be detected. Rather they are identified by tracking their decay products. The mass of the decaying particle (resonance) is the total energy of these products as measured in its rest frame. Due to its short lifetime, the uncertainty in its mass ($\sim \frac{\hbar}{\Delta t}$) is sufficiently large to be directly observable.

In this dissertation each resonance will be characterized by its isospin I, total angular momentum J, parity P, and mass M_R. Since most of the nucleon resonances have been observed in pion-nucleon scattering, the orbital angular momentum of the pion-nucleon system is often used instead of the parity. A resonance state with isospin I and angular momentum J, producing a pion-nucleon system with the orbital momentum L is denoted $L_{(2I)(2J)}(M_R)$. In this notation $\Delta(1232)$ is $P_{33}(1232)$.

Nucleon resonances are excited states of the nucleon. States with isospin $I = \frac{3}{2}$ are usually called 'Delta'-resonances (they span the entire first, second and third resonance regions) while states with isospin $I = \frac{1}{2}$ are called N^*-states (mostly in the second and third resonance regions). Our project constitutes data in the second and third resonance regions which consist of many overlapping N^* and Δ resonances, with the N^*-states having greater branching fractions into our channel.

One can describe the pion electroproduction process through the virtual photon excitation of nucleon resonances, N^*, and their subsequent decays

into mesons (both pseudo-scalar and vector mesons) and lower lying resonances, $N^{'*}$, as shown in the second Feynman diagram in Figure 2.1. Thus the excitation mechanism involves both reaction dynamics and hadron structure, intermixing quark and meson degrees of freedom. The understanding of these resonant and non-resonant components requires a variety of theoretical approaches amongst which are those listed in Section 2.2.

High precision electroproduction experiments have been used to test the predictions of these theories with unprecedented accuracy. The most precise measurements exist for excitation energies around the $\Delta(1232)$ or $P_{33}(1232)$ resonance.

The isospin ($I = \frac{1}{2}$) resonances favour the decay into the $\pi^+ n$ channel, and the measurement of $p(e, e'\pi^+)n$ is crucial for the determination of the electroproduction amplitudes for the transitions into the excited states in the second and third resonance regions.

The second resonance region is dominated by $P_{11}(1440)$, $S_{11}(1535)$ and $D_{13}(1520)$ resonances. The structure of the $P_{11}(1440)$, "Roper" resonance, is currently a subject of debate. In the constituent quark model [8] it is identified as a radially-excited three quark state with the radial excitation number $N = 2$. But in order to get the mass consistent with the experimental value, a large pertubation is introduced, which makes the application of perturbation theory unjustified. On the other hand, QCD-inspired models

predict the existence of the so-called hybrid states, where in addition to the constituent quarks there is at least one constituent gluon. For instance, in the flux tube model [19] this kind of state can be created by exciting the flux tube between two quarks in a nucleon. A hybrid state would have the same quantum numbers, but the internal structure would be entirely different from the corresponding three quark state. Current experimental data do not allow us to distinguish between the two models for the Roper resonance. Because of the isospin ($I = \frac{1}{2}$, $I_z = \frac{1}{2}$) nature of the P_{11}^{+}(1440) resonance, the $n\pi^{+}$ channel adds much sensitivity to the photocoupling amplitude.

The third resonance region is also dominated by many overlapping nucleon resonances such as the S_{11}(1650), D_{15}(1675), F_{15}(1680), D_{13}(1700) and P_{11}(1710). The study of these higher mass resonances will provide information to obtain a better understanding of nucleon structure and strong QCD.

2.3 Existing Experimental Data

Most of the existing single pion electroproduction data on proton targets are from the neutral pion channel. One of the first experiments to study charged pion electroproduction in the resonance region was conducted at the Daresbury Nuclear Physics Laboratory in the early 1970s [20]. The detector consisted of two spectrometers with approximately 2 msr angular

acceptance each. The Q^2 range was from 0.36 GeV^2 to 0.46 GeV^2, while the W range was 1.40 GeV $\leq W \leq$ 1.86 GeV and was correlated with Q^2. The angular coverage in the center-of-mass frame in θ was up to 75^0.

Another cross section measurement with forward angular coverage was conducted at Bonn University [21] at $Q^2 = 0.15$ GeV^2 and 0.3 GeV^2 in the first resonance region. This experiment used a two-arm detector as well, and the Q^2 values were correlated with W. The angular range in the center-of-mass of the hadronic system was up to $\theta = 40^0$, with 1.14 GeV $\leq W \leq$ 1.28 GeV. A few years later the Bonn group conducted another experiment [22] to study the charged pion electroproduction in the second and third resonance regions using essentially the same detectors. Measurements were done in the forward $1 \leq \cos\theta \leq 0.97$ and backward $-1 \leq \cos\theta \leq -0.97$ regions at $Q^2 = 0.3$ GeV^2. The advantage in measuring in the backward direction is that the t-channel background is much smaller at large angles.

Recently with the CLAS detector in Hall-B of the Jefferson laboratory, measurement of the single π^+ electroproduction cross sections covering nearly the full angular range in the center-of-mass frame have been carried out but for $Q^2 \leq 4.5$ GeV^2 with 1.08 GeV $\leq W \leq$ 1.70 GeV [23, 24].

The Hall-C Baryon data has provided us with the opportunity to measure the cross section of this exclusive process at the highest Q^2 of 5.5 GeV^2 with 1.3 GeV $\leq W \leq$ 2 GeV at forward angles. This will serve to constrain the

behaviour of current models that attempt to fit the world data, ours included. Since our data has extended the kinematic region where the fit must comply.

Chapter 3

Experimental Apparatus

3.1 Overview of the Experiment

The data which we worked on from experiment E01-002 performed in Hall C of Jefferson Lab was for an average Q^2 value of 5.36 GeV^2, with an electron beam energy of 5.5 GeV. This electron beam was incident on a liquid hydrogen target of diameter 4 cm, supplied by a cryogenic loop, in an evacuated scattering chamber. The Short Orbit Spectrometer, or SOS, was used to detect scattered electrons while the coincident electroproduced pions were detected at the High Momentum Spectrometer, or HMS, (see Figure 3.1). At this Q^2 value, the electron spectrometer was fixed in both angle and momentum, thus defining a central three-momentum transfer **q**. The vector **q** in turn substantially determined the direction of the pion decay cone. The pion spectrometer was stepped in angle and in momentum to capture as much of this decay cone as possible. The table below gives the spectrometer settings for the E = 5.5 GeV data.

Table 3.1: *Spectrometer settings.*

Electron Arm		Pion Arm	
P_{SOS} [GeV]	θ_{SOS} [degrees]	P_{HMS} [GeV]	θ_{HMS} [degrees]
1.74	47.5	2.13	22.5, 19.5, 16.5, 13.5
		2.23	21, 18, 15, 12
		2.57	22.5, 19.5, 16.5, 13.5, 11.2
		2.69	24, 21, 18, 15, 12
		3.10	22.5, 19.5, 16.5, 13.5, 11.2
		3.24	24, 21, 18, 15, 12
		3.73	22.5, 19.5, 16.5, 13.5, 11.2
		3.90	21, 18, 15, 12
		4.50	19.5, 16.5, 13.5, 11.2
		4.69	18, 15

To separate electrons from negatively charged pions at the electron spectrometer (SOS), both a threshold gas Čerenkov detector and a lead-glass calorimeter were used. Protons were separated from positively charged pions in the pion spectrometer (HMS) using a combination of coincidence time and time of flight, TOF, explained in detail in Section 5.2.1.

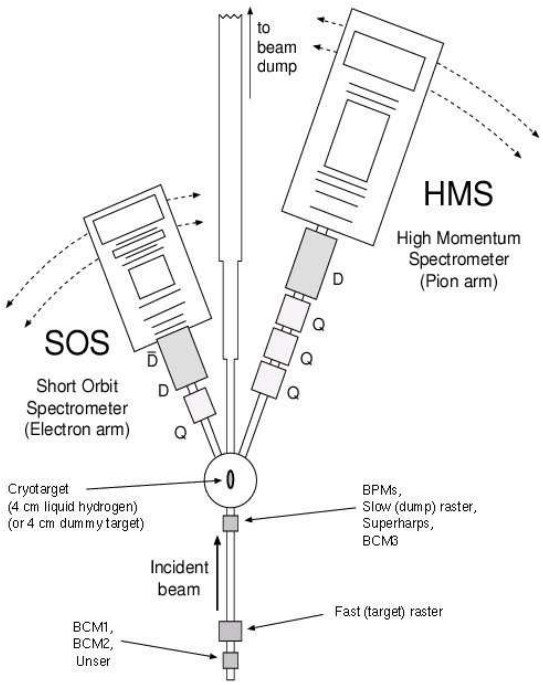

Figure 3.1: *Plan view of the experimental setup. The electron beam enters from below, and the scattering takes place in the cryogenic target placed in the beam line. The outgoing particles were detected by two magnetic spectrometers: the Short Orbit Spectrometer (SOS) was used to detect electrons and the High Momentum Spectrometer (HMS) was used to detect pions. Q are the horizontally-focusing quadrupole magnets while D are the edge-focusing dipole magnets. Figure from Ref. [1].*

3.2 The Accelerator

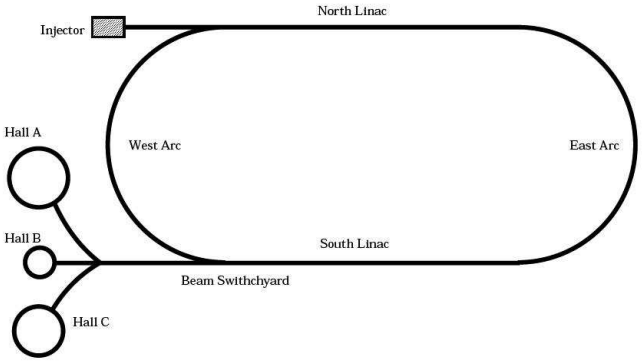

Figure 3.2: *A schematic of the CEBAF accelerator. Figure from Ref. [34].*

Jefferson Lab is an intermediate energy nuclear facility, consisting of three experimental halls (A, B, and C) that use the electron beam provided by the "continuous wave" electron accelerator to study different aspects of physics.

The Jefferson Lab accelerator is in an oblong loop configuration with a pair of linear accelerators situated on the two straightaways. A schematic of the site layout of the accelerator is shown in Figure 3.2. Electrons are accelerated by means of superconducting radio-frequency cavities in pulses at a frequency such that beam delivered in the three experimental halls are quasi-continuous. These electrons are injected into the North linac at 61.19 MeV, gain an additional 543 MeV, undergo a 180 degree bend, and again acquire another 543 MeV in the South linac. At this stage the beam can

either be sent to the Beam Switch Yard where it can be distributed to the three experimental halls or recirculated through the west arc for an additional pass through the linacs. Each linac consists of 20 cryo modules, each of which contains eight superconducting niobium cavities cooled by liquid helium at 2 K. Higher electron energies are achieved using the same linacs but separate beam pipes (beamline) in the recirculating arcs and increasing the number of trips round the loop. There are five beam pipes in the east arc and four in the west arc. Thus, the beam can be recirculated up to five times before it is sent to any of the experimental halls. The present data was taken for 5 passes (1086 MeV of energy for each pass) resulting in a high beam energy of 5.5 GeV for an average value of Q^2 = 5.36 GeV^2. Currently the accelerator is capable of delivering continuous electron beam energy of approximately 6 GeV. There are plans for a 12 GeV upgrade and an additional experimental hall D.

It should be noted that the continuous wave beam is not actually continuous, but contains an intrinsic 2 ns microstructure [1] that becomes handy when considering the accidental coincidence rate, for such a coincidence experiment.

3.3 The Hall C Beamline Instrumentation

The beam is delivered through an arc into Hall C (see Figure 3.3). This arc is equipped with a number of dipole and quadrupole magnets to steer and focus the beam. There are several monitors in the arc and in the beamline inside the hall to measure the position, profile, and current of the beam.

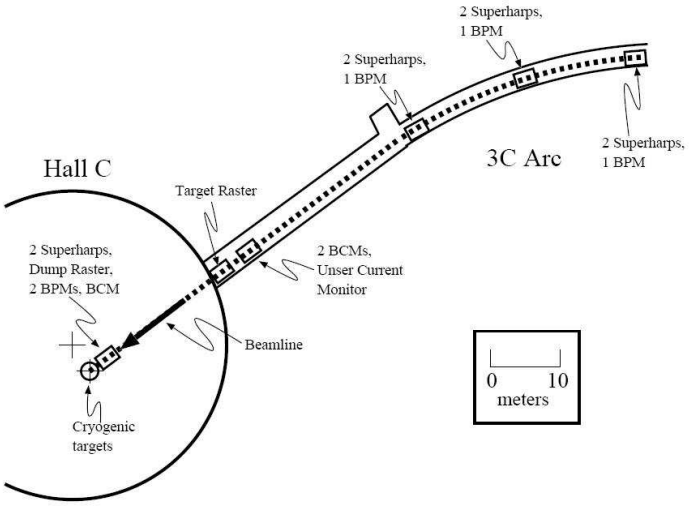

Figure 3.3: *A schematic showing placement of the Hall C beamline instrumentation. Figure from Ref. [4].*

The superharps along the Hall C arc and beamline were used to monitor the beam profile. The harp system consists of a non-fixed frame with three wires, one horizontal and two vertical. During a "harp scan" the different oriented wires move across a low current beam. An analog to digital converter recorded the signals generated at each wire when intercepted by the beam while a position encoder was used to determine the corresponding

position of the wire intercepted. These together scan the beams profile and position with a good resolution of about 10 μm.

Beam Position and Beam Current Measurements

Five beam position monitors (BPM) are used to monitor the position of the beam in the Hall C arc and the beamline. The BPMs in the arc are used typically to guide the beam while those closest to the target were monitored to ensure consistency of the position and angle of the beam on the target. The nominal beam position was set on BPMs based on information from spectrometer optics data. The typical size of the variation of the beam position at the target was less than 0.5 mm.

Three resonance-cavity beam current monitors (BCM) periodically calibrated by an Unser current monitor perform nondestructive measurements of beam currents during data taking. Detailed documentation of the beam position, beam current measurements and the calibration of the BCMs can be found in Refs. [4, 25, 26].

The beamline is also equipped with a pair of fast raster magnets. Their purpose is to reduce the damage that can be caused from local heating during the experiment. The beam was rastered to a 2×2 mm profile to distribute the energy in a more uniform manner over the cryotarget volume. The two fast raster magnets steer the beam in a sinusoidal pattern in both the vertical and horizontal direction.

Beam Energy Measurement

The energy of the electron beam sent to Hall C is measured by using the arc as a spectrometer [27]. For the energy measurement only the dipole magnets inside the arc are energized to bend the beam, the other magnets are degaussed in order to minimize residual fields. A couple of dipole corrector magnets are left on to correct for the earth's field. The position and direction of the beam is measured using BPMs or Superharps at the entrance and the exit of the arc. This knowledge is combined with the well known field integral $\int B{\cdot}dl$ of the arc dipoles as a function of the current [28] to calculate the electron energy via the relation:

$$p = \frac{e}{\theta_{arc}} \int B \cdot dl, \tag{3.1}$$

where p is the particle momentum, e is the electron charge and θ_{arc} is the bend angle of the arc (34.3^o). More detailed discussions of this technique can be found in Refs. [29, 30, 27].

3.4 The Cryogenic Target

To achieve reasonable rates of data-taking in Hall C, use is made of dense targets that optimize the experimental luminosity. To this effect, the target nucleus in this experiment was hydrogen provided in liquid form in a

loop with circulation maintained by an axial pump. The liquid hydrogen was cooled by helium supplied at a temperature of 15 K using a heat exchanger. The liquid target was maintained at 19.00 K by using a calibrated heat-dependent resistor in the feedback loop of a dual-resistive-heater temperature system.

In addition to the liquid cryogenic target, in the cryogenic target stack, were two aluminium and five carbon foils located at different z-positions along the beam direction. The target stack was raised or lowered by an actuator in order to put the appropriate target cell in the beamline. The aluminium slabs constitute the "dummy target" used to subtract the aluminium can contribution to the cryotarget yields. This dummy target was approximately seven times thicker than the hydrogen target cell walls, of ≈ 0.0127 cm, in order to reduce the time needed for background measurement. On the other hand, beam incident simultaneously on two or all five of the solid carbon foils are used for calibrations and optics tests.

Additional information about the cryogenic target system can be found in Refs. [31, 32, 33]

3.5 Spectrometers

Particle detection is one of the most critical pieces in an experiment of this nature. Experiment E01-002 made use of the two standard Hall C magnetic

spectrometers. The Short Orbit Spectrometer (SOS) was designed and built to detect short-lived particles, hadrons, such as pions and kaons. This is accomplished by making the distance to the focal plane relatively short ($\approx$ 10 m) in order to minimize decay losses. On the other hand, the High Momentum Spectrometer (HMS) has a greater distance to the focal plane ($\approx$ 25 m) making it more suitable for detection of electrons. For experiment E01-002, the HMS was used for hadron detection - since the hadrons in this case are at very high momentum such that it was not possible to use the SOS. Also at higher momentum, decay losses are not such a large factor [34].

3.5.1 The Electron Arm Spectrometer

As indicated, the Hall C Short Orbit Spectrometer (SOS) was used to detect outgoing electrons. This device was also designed to have large acceptance in both scattering angle and momentum. To this end, the device consists of a horizontally focussing quadrupole followed by two edge-focussing dipoles, the focus is transverse to the dispersive direction. Changes in spectrometer rotation and magnetic field were made remotely from the counting room.

The spectrometer solid angle was determined by an octagonal collimator which defines a maximum angular acceptance of approximately 7 msr in total solid angle. The collimator apertures for both electron and pion spectrometers were made with an angle, so that the edges were parallel to the rays coming from the point target. In addition to the octagonal collimator,

there was a sieve slit (a collimator with many small holes) which was used to find the matrix elements of the focal-plane-to-target transformation [4].

The SOS was equipped with two pairs of scintillator arrays, two drift chambers, and a threshold gas Čerenkov detector.

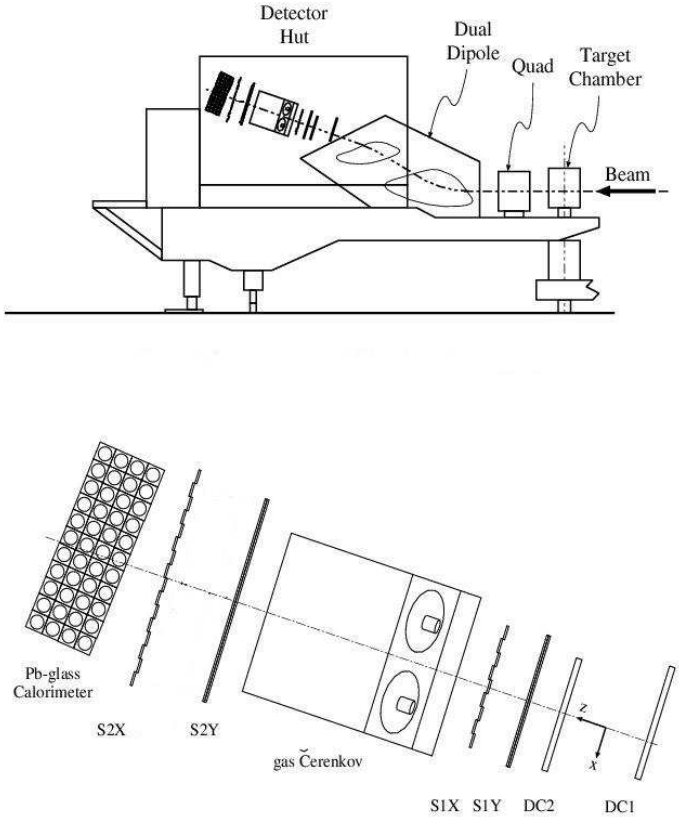

Figure 3.4: *A side view of the SOS and its detector stack. Figure from Ref. [4].*

The SOS Magnetic Elements

The setting procedure for the SOS magnets is of great importance for determining momenta and reconstructed parameters. The quadrupole and the two

dipoles are all non-superconducting , and are cooled by pressurised water. The fields for the magnets were measured by Hall probes situated in regions where the magnetic field was uniform. The magnetic fields were remotely set from the counting room. In general the magnets were operated such that they began in a demagnetized state and care taken for them to always be on the part of the hysteresis curve of increasing current. When a decrease in current was necessary, the magnets were first demagnetized and the desired field approached from below. The kinematics for this experiment called for a single SOS magnet and angle setting at each of two Q^2 points, and care was taken not to change the field setting during data taking.

The SOS Scintillator Arrays

Charged particles traversing a scintillating material ionize atoms, thereby liberating electrons in the medium. These electrons interact with the scintillating medium and excite molecules to higher energy levels. When these excited molecules spontaneously return to their ground states, they emit light. The emitted light propagates through the medium by total internal reflection and is detected by photomultiplier tubes (PMTs) on either end attached to a lucite light guide. To ensure light-tightness, scintillator elements are wrapped in layers of dark Tedlar.

The SOS detectors included four planes of slightly overlapping scintillator strips, equipped at each end with light guides and PMTs, two towards

the front of the detector stack and two towards the rear (see Figure 3.4). The first plane encountered by a particle, S1Y, had 9 scintillators arranged along the x (dispersive) direction. The second plane, S1X, had 9 scintillators arranged in the y (nondispersive) direction. Towards the rear of the detector hut this arrangement was repeated with planes S2Y and S2X (9 and 16 scintillators, respectively). The scintillator planes serve a dual purpose: triggering of the data acquisition system and measurement of particle velocity using time-of-flight from the front to the rear of the detector hut. A plane recorded a hit whenever an above-threshold signal from any PMT on one side of the plane arrived within about +60 ns or -60 ns of a signal from the opposite side of the plane. In the Hall C counting house (electronics room), the Experimental Physics Industrial Control System (EPICS) was used to supply, monitor and control the high voltage for the PMTs [35]. The analog signals coming from the PMTs were routed directly up to the electronics room. Once there, the analog signal from each of the PMTs was split by 2:1 voltage divider. The smaller signal went to an analog-to-digital converter (ADC), the output of which was used to make pulse-height corrections to the timing. The larger signal was discriminated, and the resulting logic signal was sent to a time-to-digital conveter (TDC), a scaler, and to the logic devices that formed pretriggers.

The SOS Drift Chambers

The principle of operation of particle tracking drift chambers is as follows. A chamber is filled with some gas mixture, while some number of layers of field and sense wires are also positioned inside the chamber. When a charged particle traverses the chamber, the gas (or gas mixture) is ionized thereby liberating electrons. The liberated electrons are then accelerated due to a (negative) potential difference between the sense and field wires - these electrons are then detected at the sense wires and read out as a current over a period of time. While the wire spacing itself gives some information regarding the trajectory of the track, the large wire spacing limits the precision. However, timing information (with respect to the trigger) can be used to increase the precision. If one measures the time that it took for the liberated electrons to reach the sense wires, one can then convert this to a distance and determine how far the track of a charged particle was from a given wire. To minimize the effect of multiple-scattering in air and the vacuum window, the first detector modules encountered by a particle were the drift chambers (DC1 and DC2). Two separated drift chambers each consisting of six planes of sense wires were used to reconstruct the track in the SOS. The order of the planes and the relative orientation of the wires in different planes are shown in Figure 3.5. The gas used in the drift chambers was an Argon-Ethane mixture controlled by a gas mixing system located

above the experimental hall. The ethane acted as a quenching agent to decrease the electron drift velocity and hence increase the spatial resolution [36].

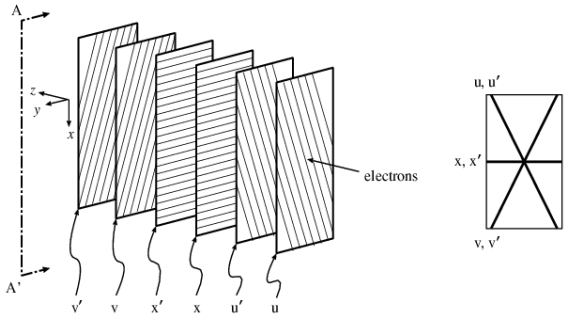

Figure 3.5: *Orientation of wires in the SOS DC1 as seen by the incoming electron. Figure from Ref. [4].*

The spacing between the sense wires was 1 cm (see Figure 3.6). The field wires and inter-plane foils were kept at high voltage, while the sense wires were held at ground. The primed (x',u',v') and the unprimed (x,u,v) planes were offset by 5 mm in order to help remove the left-right ambiguity inherent in the drift-time measurement of a single plane.

The SOS Gas Čerenkov Detector

The SOS had a threshold gas Čerenkov detector designed to distinguish electrons from negatively charged pions. The Čerenkov detector monitors the radiation emitted when a charged particle traverses the medium (with index of refraction n) in the detector with velocity (β) which is faster than the speed of light in that medium (c/n). The light will be emitted with

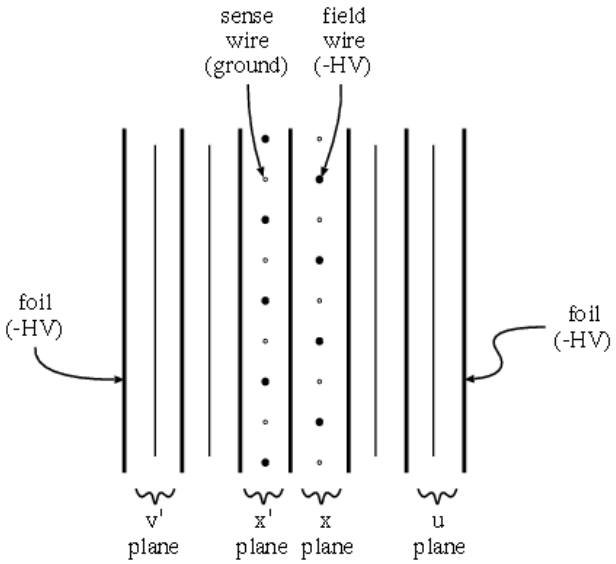

Figure 3.6: *Cross section of a single SOS drift chamber. Figure from Ref. [4].*

angle $\theta_c = \arccos(1/n\beta)$, which for fast particles and n close to one is a very small angle. This light is then reflected from parabolic mirrors in the detector and focussed onto four photomultipliers tubes.

The threshold property of Čerenkov radiation makes it possible to tune the medium in the detector to allow for specific conditions like electron and pion selection and their separation over a particular momentum range. The Čerenkov medium was Freon-12 at a pressure of one atmosphere. At this pressure, the refractive index of Freon-12 is 1.00108 which results in an electron threshold of 11 MeV/c and a pion threshold of 2.95 GeV/c. Although the separation of electrons and pions is very efficient, pion rejection is complicated by the presence of knock-on electrons (giving mostly small

pulse heights). These knock-on electrons are produced when a pion interacts with the material in front of the Čerenkov gas volume and can subsequently result in a hit in the Čerenkov detector. The mis-identification of pions due to knock-on electrons was not a significant effect in this experiment.

The SOS Lead-Glass Calorimeter

At the rear of the SOS detector hut was an array of 44 blocks of lead glass, each 10 cm by 10 cm by 70 cm long, stacked 11 blocks high by four blocks (16 radiation lengths) deep. Each block was equipped at one side with a photo multiplier tube (PMT) (see Figure 3.4). The entire structure was tilted 5 degrees with respect to the spectrometer central ray to prevent the propagation of particles through the gaps between the blocks. The lead glass collected the Čerenkov light which can be emitted by the primary particle traversing the detector, or knock-on electrons, or an electron or positron produced in one of the stages of the electromagnetic shower caused by a primary electron. The measurement of the total energy deposited in the lead glass detector allows the discrimination between electrons and negative pions since the amount of light produced by the electron is significantly larger than that of a pion which has a very small probability to deposit its full energy by producing the neutral pion via the charge exchange nuclear interaction i.e. $\pi^- p \rightarrow \pi^0 n X$ and the subsequent decay of the π^0 to two gammas ($\pi^0 \rightarrow \gamma\gamma$) which make electromagnetic showers.

3.5.2 The Pion Arm Spectrometer

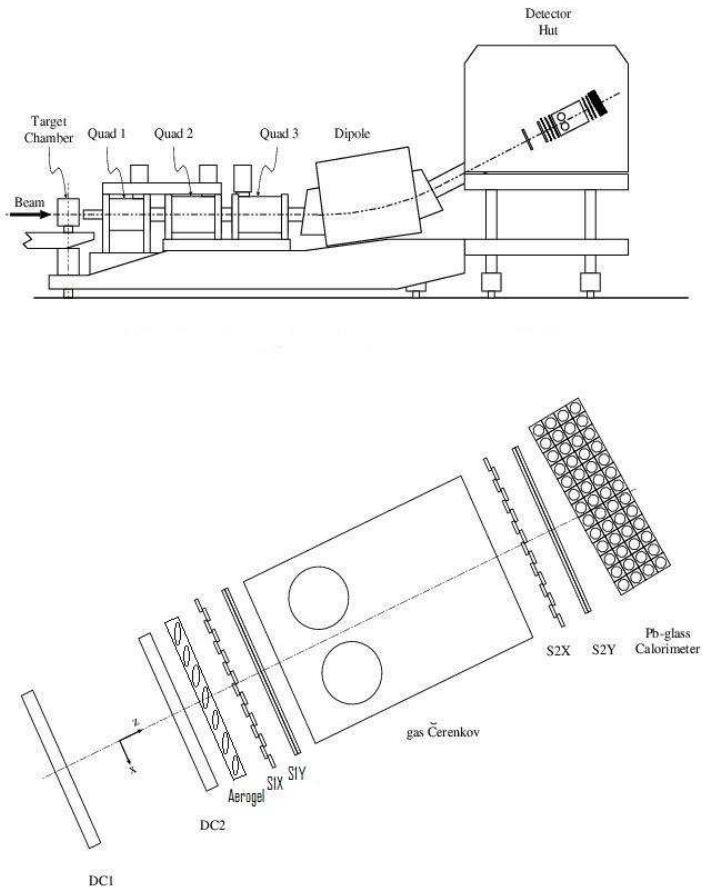

Figure 3.7: *A side view of HMS and its detector stack. Figure adapted from Ref. [4].*

The Hall C High Momentum Spectrometer (HMS) was used to detect outgoing pions (see Figure 3.7). The HMS consisted of three superconducting quadrupoles followed by a superconducting dipole that bends in the dispersive direction and determines the central momentum of the spectrometer. Changes in spectrometer rotation and magnetic field were made

remotely from the counting room.

The solid angle, as with the case of the SOS spectrometer, was determined by an octagonal collimator positioned between the target and the first quadrupole magnet. The collimator defines a maximum angular acceptance of 6.8 msr.

After passing through the magnetic field, particles were detected by the focal plane detector. But for the extra aerogel detector, the HMS package was similar to that in the SOS. The HMS was equipped with two pairs of scintillator arrays, an aerogel detector, two drift chambers, a threshold gas Čerenkov detector, and a lead-glass electromagnetic calorimeter.

The HMS Magnetic Element

The magnetic settings are crucial in defining the momentum of the spectrometer and hence the reconstruction of detected particle tracks. The HMS is in a Quad-Quad-Quad-Dipole configuration. The magnetic fields were set remotely from the counting room. Whereas the quadrupoles were regulated by current, the field of the dipole was regulated using the output from an NMR (nuclear magnetic resonance) probe located in a region of uniform field.

The power supply readback current and Hall probes were used to monitor the quadrupoles. The normal use of the magnetic field from the Hall probes is to ensure that the same relative field values result from similar set

currents.

The HMS Scintillator Arrays

The HMS, like the SOS, had four planes of scintillators, two towards the front of the detector stack and two towards the rear. Each plane consisted of staggered, slightly overlapping strips of scintillator equipped at each end with light guides and PMTs. The first plane encountered by a particle, S1X, had 16 scintillators arranged along the y (dispersive) direction. The second plane, S1Y, had 9 scintillators arranged in the x (nondispersive) direction. Towards the rear of the detector hut this arrangement was repeated with planes S2X and S2Y, respectively.

The scintillator planes served two purposes: triggering of the data acquisition system and measurement of particle velocity using time-of-flight from the front to the rear of the detector hut.

The HMS Drift Chambers

Two drift chambers (DC1 and DC2) were used to provide track information for events in the HMS. Each chamber consisted of six planes of sense wires oriented as shown in Figure 3.8.

The spacing between the sense wires was 1 cm. The field wires were held at negative high voltage, while the sense wires were grounded (see Figure 3.9). For the same reason as in the SOS drift chambers, the unprimed

and primed planes were offset by 5 mm. The chambers were located at the front of the detector stack to minimise the effect of multiple-scattering in the preceding vacuum window and air.

The gas used in the drift chambers was the same argon-ethane mixture as that used in the SOS.

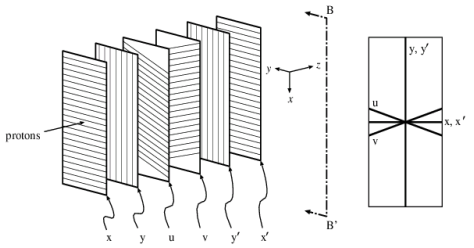

Figure 3.8: *Orientation of wires as seen by the incoming pion. Figure from Ref. [4].*

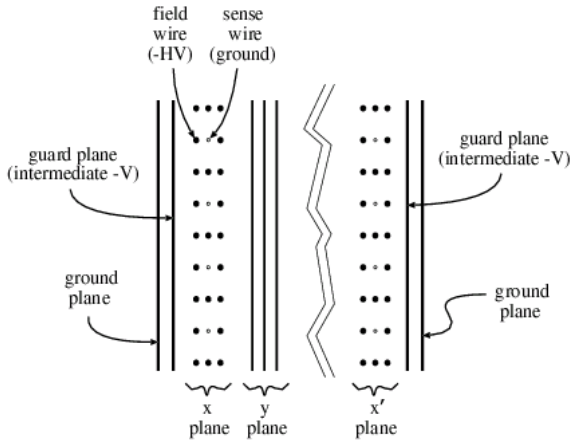

Figure 3.9: *Cross section of a single HMS drift chamber. Figure from Ref. [4].*

The HMS Gas Čerenkov Detector

The HMS Čerenkov detector is a cylindrical tank holding two mirrors and two PMTs. The detector is designed in such a way as to allow for gas pressures in the tank equal to or above and below the atmospheric pressure. Hence, the detector is limited to π/e separation at atmospheric pressure or below, but it can also be used to separate pions from protons using Freon-12 at very high atmospheric pressures.

The HMS Aerogel Čerenkov Detector

As seen in Table 3.1, the central HMS momenta at some spectrometer settings were well above 3 GeV. For this reason an aerogel threshold Čenrenkov was used at the HMS to provide adequate separation of pions and protons at such high momenta. At high momenta it is not possible to separate pions and protons by a direct measurement of the particle velocity due to the decrease in the time-of-flight resolution ($\Delta t \approx 1/P^2$). The principle of particle detection with the aerogel Čerenkov is also based on threshold Čerenkov radiation, that depends on the refractive index of the medium.

Aerogel is a hydrated silicon oxide of molecular structure n(SiO_2) + 2n(H_2) and density ranging between 0.04 and 0.20 g/cm^3. The hydrate surrounding the molecule allows aerogel to assume a mean refractive index between gases and liquids. Two configurations of refractive indices 1.030

and 1.015 are available. The aerogel with refractive index of 1.030 gives a pion threshold of 0.565 GeV and a proton threshold of 3.802 GeV.

Details on the design and testing of the aerogel Čerenkov detector can be found in [37].

3.6 Trigger and Data Acquisition

A key element in an electroproduction experiment of this nature is the event trigger. For this experiment the trigger was set up as a coincidence between the two single arm pretriggers. The net rate of paticles entering the spectrometers can be quite large and one needs to discriminate real events from events that are partially accepted (i.e. give signals in one or more detectors but not enough to be a good event). A good trigger balances discrimination with high efficiency. In Hall C, the HMS and SOS each have their own event selection criteria. Once passed, the so-called singles pretrigger is formed if 3 out of 4 of the scintillator planes fire in each spectrometer. The pretrigger signals were passed to coincidence electronics. The timing between the SOS and HMS pretrigger and their widths were adjusted to allow a coincidence window of 60 ns.

The data acquisition (the recording of data as well as the user interface) was handled by the CODA (CEBAF Online Data Acquisition) software package [38]. Data for each run was written directly to disk and con-

sisted of three types of events: 1) detector information handled by the ADCs and TDCs; 2) scaler information; and 3) information from EPICS database.

The data we have used for this dissertation was acquired for seven weeks of beam time and a full set of consistency checks for the data have been made.

Chapter 4

Simulation of the Experiment

4.1 Overview of the Hall C Monte Carlo

SIMC is the standard Monte Carlo program used in Hall C. The simulation includes the Hall C coordinate system and Monte Carlo simulations of the present and future Hall C spectrometers. Though SIMC does not have the capability to simulate individual detector signals, it however includes all relevant details of the experimental conditions that ensure a realistic simulation of experimental data, such as, rastering and energy spread of the electron beam, radiation processes, hadron decay and finite track resolution. SIMC is currently set up to simulate processes such as (e, $e'p$) from Hydrogen, Deuterium, Carbon, Iron, and Gold targets as well as (e, $e'\pi$) type reactions (meson electroproduction) from Hydrogen, Deuterium and Helium-3 targets. Experiments such as Ref. [39, 34, 1] have used SIMC for the analysis of pion electroproduction data.

Before entering the main event loop, the Monte Carlo generates, for each

real event, both the initial coordinates of the interaction and kinematic properties such as direction and momentum of the particles of interest. Typically, the generation limits in kinematics fixed by an input to the simulation are chosen to exceed the physical acceptance of the spectrometers. SIMC takes the generation limits given, and increases them so that the outgoing event is radiated and followed on its course through the target with energy loss and multiple scattering taken into consideration. After the event generation, the events are sent to the single arm codes which simulate the magnetic optics inside the Hall C spectrometers and propagate the particles through apertures and magnets into the detector hut. Inside each hut a particle's trajectory is measured at each detector aperture. Events that go through all apertures and cross a minimum number of detectors in the huts are considered successful and hence will produce a valid trigger. Each time a valid trigger is generated, all physical variables of the particle needed for further analysis are reconstructed to the target and written to a file. Successful events are weighted by the relevant model cross section corrected for radiative processes, a luminosity factor, and a Jacobian taking into account the transformation between spectrometer and physics coordinates. The spectrometer is in the lab frame while the event generator is in the centre-of-mass system.

4.2 Event Generation

A straightforward implementation for pion electroproduction from hydrogen can be done by SIMC. The Monte Carlo must generate five quantities that correspond to the five-folded cross section of the process. The chosen variables are the spectrometer in- and out of plane angles for both the electron and the pion arms, as well as the final electron energy. All of these quantities are simulated with a uniform (flat) distribution with limits not strictly fixed by the spectrometer acceptance so as to allow for multiple scattering and energy loss as indicated earlier. With the five variables specified, the kinematics are totally determined and the pion momentum calculated from energy-momentum conservation.

After the generated variables and the pion momentum have been specified, the five fold pion electroproduction cross section can be calculated. As described in Chapter 1, for a simulated event in SIMC, the model pion electroproduction cross section is written in terms of the virtual photon flux (Γ) and the center-of-mass photoproduction cross section ($d\sigma/d\Omega_\pi$), Equation (1.2). Since the quantities generated in SIMC are done in the lab frame, one needs a Jacobian that will transform the photoproduction cross section into the center-of-mass frame, Ref [34]. The derivation of this Jacobian makes use of fact that energy and momenta are independent of the pion angle in

the center-of-mass frame.

4.3 Spectrometer Models

Events are sent to the single arm Monte Carlo after their angles and momenta have been generated at the vertex. Here the particles are followed through the collimators and the spectrometer magnets to the wire chambers and other detectors using the COSY INFINITY model [40]. The model of the magnets in the spectrometers is generated using field map data in comparison with actual data. COSY generated matrix elements are used for both spectrometers to trace the particles sequentially (step-like) through the magnetic fields and apertures inside the spectrometers. Implementing the COSY model sequentially (e.g. in the HMS, one might transport a particle from the target to the entrance of the first quadrupole, from there to the middle of the first quadrupole and so on) is advantageous in terms of allowing for the modeling of pion decay.

4.4 Passage Through Materials

Including multiple scattering and energy losses as particles go through various materials at different kinematics enables SIMC to model particle events realistically.

4.4.1 Multiple Scattering

It is necessary to simulate the effect of Coulomb multiple scattering in the target and the spectrometers in order to better match the resolution of the data. The change in the original scattering angle of a particle after traversing a certain material (or combination of materials) can be calculated from a random Gaussian distribution number, g, and the width of the multiple scattering Gaussian distribution, θ_{rms} :

$$\Delta\theta = g\theta_{rms} \tag{4.1}$$

with θ_{rms} given by

$$\theta_{rms} = \frac{13.6\sqrt{t}[1 + 0.038\ln(t)]}{\beta p} \tag{4.2}$$

where β and p denote the speed and momentum of the incident particle in units of MeV and t is the thickness of the scattering material in radiation lengths.

For all atomic number, Z, and $\beta = 1$ particles, the parameterization of θ_{rms} has been shown to closely agree with calculations of Molière scattering [41] used by SIMC. Tests indicate that changing the width of the distribution

by as much as a factor of two has negligible impact on the number of events accepted by the Monte Carlo.

Multiple scattering is calculated in SIMC for both the incoming and outgoing electrons and also for the produced pion. The effect of the incident electron multiple scattering is modeled by applying a correlation modification to the scattered electron and outgoing pion.

4.4.2 Ionization Energy Loss

Ionization of atoms in the thick cryogenic target and the target can cause energy to be lost by the incident and scattered electron and the pion. Although the Bethe-Bloch equation (see [41]) is a good parameterization of the average energy loss by charged particles in matter, a Landau distribution is preferable since it can take into account fluctuations around the average energy loss [42]. In SIMC, the Landau distribution is used to calculate this average energy. The energy loss distribution is characterized by the most probable energy loss, E_{prob}, and the full width at half maximum of the distribution, ξ.

The most probable energy loss can be calculated from the true energy loss and a random number λ,

$$E_{prob} = E_{true} + \lambda\xi \tag{4.3}$$

where $\xi = K\frac{Zt}{A\beta^2}$ (K = 0.15354 MeV cm^2/g). β denotes the velocity of the incident particle in units of c, Z and A are the atomic and mass number of the material, and t is the material thickness in g/cm^2. Details on how the Landau distributed random number is obtained is outlined in Refs. [34, 43].

SIMC calculates the relevant energy loss of the incoming electron as it passes through the aluminium can of the cryogenic target as well as the target and its exit window. Calculation of energy loss is also done for the outgoing electron and the pion as they pass through the remaining part of the target, the target can, the scattering chamber and the spectrometer window. The general procedure is consistent with the one used in the data analysis (see [43]) with regards to correcting the incident and scattered electron energies as well as the hadron energy for energy loss in the reconstruction of events. Nevertheless, while SIMC calculates the most probable energy loss, the data analysis applies the average value of the energy loss. The difference in the correction is relatively small such that it does not affect the comparison of simulated and experimental data.

4.5 Pion Decay

The sequential forward COSY generated matrix elements in the single-arm Monte Carlos includes the simulation of the decay of pions in flight into

muons and muon neutrinos. The branching ratio of charged pions decaying via this channel ($\pi^{\pm} \rightarrow \mu^{\pm}\nu_{\mu}$) is very close to unity. Usually, some pions that decay may be lost before reaching the minimum number of scintillator layers needed to produce a valid trigger.

To correct the data for pion decay, two different processes are implemented. The first correction involves correcting for the total number of events lost when the pion decays and the resulting muon is not within the acceptance of the HMS. The second situation is to implement a correction to resulting muons from the pion decay process that also trigger. Unlike the first case, implementation of the second correction is complicated in that muon tracks do not necessarily reconstruct to the true pion interaction vertex at the target, thereby distorting the distribution of reconstructed variables. This difficulty arises from the fact that the muon mass (0.105 GeV) is quite close to the pion mass (0.139 GeV) reducing the possibility of uniquely identifying and separating both particles, either using time-of-flight or some kind of calorimetry. It is therefore not feasible to eliminate all muon tracks from the data sample and use a common correction factor to account for the number of pion events.

Details of how SIMC is used to simulate pion decay, account for the number of events lost and model the muon tracks that come from these decays can be obtained from Refs. [34, 1]. In SIMC the pion can decay at

any point along its path in field free regions and at points in the magnetic fields of the HMS. A muon from a pion decay that occurred early on its path to the detectors is more likely to fail cuts on reconstructed quantities than one from a decay close to the detectors. More than 85% of all simulated muons that survive all cuts originate in the field region behind the HMS dipole. An estimated uncertainty of 1% due to the simulation of pion decay can therefore be considered safe.

4.6 Radiative Processes

One of the most important parts in analyzing electron scattering experimental data is to correct for radiation due to the emission of real or virtual photons by incident or scattered electrons or hadrons involved in the reaction. Traditionally, correction of radiation of experimental data involves calculating a correction factor in terms of missing mass at some mean Q^2 and W to account for the re-distributed strength in cross section.

However, in similar experiments where the un-radiated cross section varies quite significantly over the experimental acceptance, the implementation of radiative processes to accommodate pion electroproduction in SIMC had been made possible by the work of Mo and Tsai [44, 45]. In that work, the formalism for radiative corrections applied to inclusive elastic electron scattering from protons was modified and later on extended for use in coin-

cidence experiments [46, 47, 48]. The modification to accommodate pion electroproduction can be done in one of two ways. The first approach is to treat the target proton as a virtual pion. In the second case, the target proton is considered to be stationary and the final pion treated to be an off-shell proton. The difference between the two methods is negligible, though the second is used in this analysis.

Radiative processes in electron scattering can be classified into two types, external and internal radiation. For external radiation one of the charged particles (incoming electron, outgoing electron, or outgoing pion) in the reaction radiates a real photon upon interactions with the electric fields of nuclei encountered while traversing a material other than the target. Corrections for this type of radiation are rather simple since the particles radiate independently at some distance from the primary interaction vertex thereby independently eliminating interference terms in the summation of the amplitude. More complicated to handle are the internal effects in which either the incoming or outgoing electron or pion radiates in the field of the target nucleon. Here the amplitudes add up coherently resulting in various interference terms that must be included in the calculation (see Figure 4.1 for the first order bremsstrahlung interference terms).

Internal corrections also include second order (or hard) diagrams such as vacuum polarization and particle self energy diagrams (Figure 4.2). How-

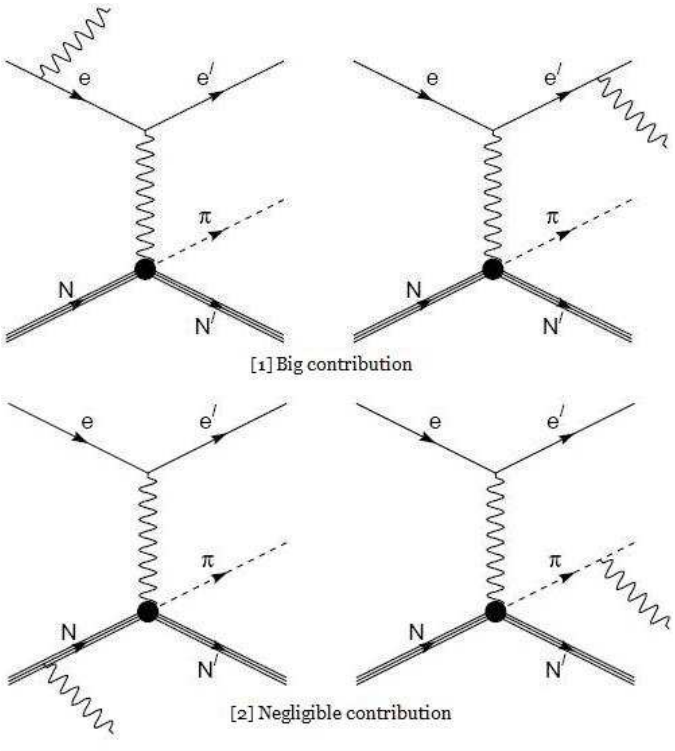

Figure 4.1: *Feynman diagrams contributing to first order, internal, soft radiative corrections. Figure from Ref. [34].*

ever, only processes that cancel infrared divergent terms from the first order corrections are kept.

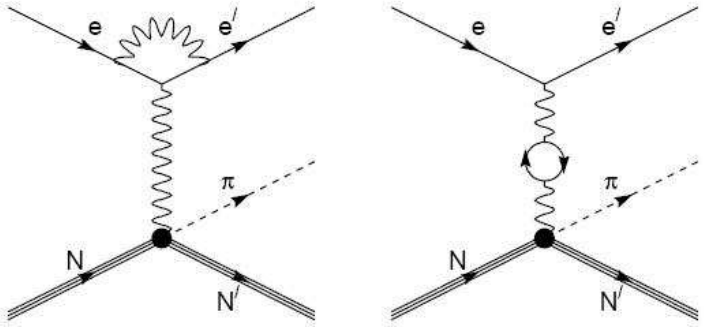

Figure 4.2: *Feynman diagrams contributing to second order, internal, hard radiative corrections. Figure from Ref. [34].*

A more elaborate description on how SIMC carries out radiative corrections can be found in Refs. [34, 1].

Chapter 5

Data Analysis

The offline data analysis of the collected raw signals was done using the dedicated Fortran based Hall C analysis code called ENGINE [49]. ENGINE reads each raw event, determines which detectors were fired, reconstructs trajectories, and generates particle identification information for each event. In effect, the replay ENGINE converts raw data into calibrated physical quantities (the physical quantities may include combinations of raw data quantities) on an event by event basis. This software interacts with two different packages:

- CODA (Cebaf Online Data Acquisition) [38] for event readout and decoding.
- CERN libraries for access to fitting, plotting and data presentation such as PAW, HBOOK etc.

During the analysis of E01-002, the signals were replayed offline a number of times using the data reduction ENGINE each time there was an improvement in the calibration of the detectors. Each replay will generate an output stored in three different forms:

1. A scaler file that consists of the beam current, detector efficiences, hardware/software scalers, and dead time correction factors.

2. A standard set of histograms files, in HBOOK format, often used to monitor the performances of the detectors during runs in the experiment, and

3. N-tuples that consists of mostly calibrated detector quantities, track quantities (position and angle of track from the focal plane of the spectrometer), as well as timing and energy deposition information. Also included are scattering quantities such as the centre-of-mass angles, the invariant mass and the missing mass when a proton is detected at the HMS.

Other analysis codes utilizing Perl and C++ in the Root Data Analysis framework, a recent high energy physics package produced by CERN (European Organisation for Nuclear Research), were developed. These codes run on both the JLab computer farm as well as on computers at the University of the Witwatersrand to process reduced data sets that are transferred

from JLab. The codes were used to convert HBOOK files into ROOT files and to calculate reconstructed and physics quantities (like missing mass, Q^2, etc.). Separating the analysis process this way has the advantage of allowing one to do local analysis which will include, amongst others, the modification of cuts, particle identification through the use of the time of flight and energy deposition information, missing mass reconstruction for pion events at the HMS, the determination of the angular distribution etc, without having to waste a lot of time doing complete replays at JLab computers. In practice, one must continually modify and develop parts of these codes in the analysis process in a cycle of computational processing of the data and discussion, in order to achieve ultimate reliable extraction of the observables from the data.

In this chapter, we shall discuss the different aspects of the data analysis done locally and the process of extracting the differential cross section by comparing the data with a Monte Carlo simulation.

5.1 Data Correction

In order for us to do appropriate analysis and rely on the results thus obtained, we need to use reliable data corrected on a run-by-run basis for track reconstruction inefficiencies, dead times and offsets. As indicated earlier, a scalar file consisting of the detector efficiencies and dead time correction

Effect	Correction in %
Pion absorption	+2.7 $\pm$ 1.3
†Computer dead time	+(1.0 - 19.1)
†HMS tracking	+(2.3 - 14.3)
†SOS tracking	+(0.3 - 0.9)
†Electronics dead time	+(0.0 - 2.4)
‡Random coincidence	-(0.0 - 7.6)

Table 5.1: *Corrections applied to the data. Parentheses indicate the range of correction sizes applied on a* †*run-by-run or a* ‡*bin-by-bin basis.*

factors for each run was generated during offline replay. Use of these files were made to correct the data for detector inefficiencies and dead times on a run-by-run basis during a procedure at which each event passing specific cuts was filled into a histogram weighted by a run dependent correction factor [50]. Table 5.1 shows all the corrections applied to the data.

Offsets to the nominal spectrometer values were determined in experiment E01-004, the pion form factor (F_{π}-2) experiment [1], that preceded this experiment with same apparatus. Experimental offsets arise when uncertainties in the fitting of the reconstruction matrix elements for the spectrometers are not considered. Since the calculation of the experimental cross sections depends on physics quantities like Q^2 and W obtained from the reconstructed spectrometer quantities (central angles and momenta) and the beam energy, it is therefore directly sensitive to uncertainties in the spectrometer quantities. In the F_{π}-2 experiment, offsets were determined

Quantity	HMS	SOS
θ	0.0 $\pm$ 0.5 mrad	0.0 $\pm$ 0.5 mrad
ϕ	+1.1 $\pm$ 0.5 mrad	+3.2 $\pm$ 0.5 mrad
p_0	-0.13 $\pm$ 0.05 %	-0.96 $\pm$ 0.05 %
E_e	0.00 $\pm$ 0.05%	

Table 5.2: *Kinematic offsets measured in the analysis of [1].*

by analysing elastic electron singles data and use of the overconstrained $^1H(e, e'p)$ reaction. The entire set of kinematic offsets, listed in Table 5.2, were used in the replay of our data.

5.1.1 Pion Absorption

One of the larger corrections is that for pion absorption in the material of the target and those of the HMS focal plane detectors. Pions may interact hadronically resulting in no pion in the final state in the case of true absorption, or may be subjected to large angle scattering resulting in pions that do not strike 3 out of 4 scintillator planes required to form a trigger.

The fraction, T, of pions that do not interact with materials on the way and through the HMS can be expressed as

$$T = e^{-\sum \lambda_i t_i} \tag{5.1}$$

where t_i denotes the thickness of the ith material encountered by the parti-

cles and λ_i denotes the material's interaction length defined by:

$$\lambda = \rho N_A \frac{\sigma_A}{A} \tag{5.2}$$

with ρ the material density, N_A is the Avogadro's number and σ_A is the relevant pion-nucleon cross section for a material of atomic mass A. Hence, given the list of the appropriate pion-nucleon cross sections and properties of materials encountered in the HMS, the pion transmission can be calculated.

A choice amongst three pion-nucleus cross sections largely determines the uncertainty in the calculated value of the pion transmission through the materials. There is

- the total cross section which is the sum of all hadronic interactions and represents the lower limit of the transmission,
- the "true" absorption cross section with no pions in the final state that represents the upper limit of the transmission and finally,
- the reaction cross section which includes all hadronic interactions except for elastic scattering ($\sigma_{reaction} = \sigma_{absorption} + \sigma_{inelastic}$).

The total cross section represents an underestimate of the transmission because elastic scattering is peaked in the forward direction such that a large

number of the elastically scattered pions would still generate a valid trigger. Moreover, a pion that scatters inelastically does not necessarily correspond to an invalid trigger. The reaction cross section is therefore used to estimate the uncertainty on pion transmission since it is roughly the average of the two limiting cases of total and absorption cross sections.

The A-dependence of the pion-nucleus cross section for large A materials ($A > 4$), can be calculated using the parameterization:

$$\sigma_A = \sigma_0 A^q, \tag{5.3}$$

where σ_0 and q are fits to experimental data. As elaborated in [1], the cross section for each material at the HMS detector hut can be calculated using some parameterization and Equation (5.3) with the corresponding length determined from Equation (5.2).

For the liquid hydrogen target ($A = 1$) the lower limit on the pion transmission could be estimated from actual total cross section data, since for $A < 3$ the A-dependence expressed by Equation 5.3 does not hold.

However, the absorption of pions was not measured directly. Instead the absorption of protons from the elastic $^1H(e, e'p)$ reaction was measured by Dalton [50] and $\frac{2}{3}$ of this value used for the pions. This is under the assumption that the total absorption cross section for pions on nuclei is about $\frac{2}{3}$ to

that for protons (as there are $\frac{2}{3}$ as many quarks in a pion as there are in a proton). Hence to account for pion absorption, a correction of 2.7% was applied to the data. The total uncertainty on the pion absorption correction can be estimated in a less conservative way from the measured proton absorption and the relative size of the proton and pion absorption cross sections. A resulting uncertainty of 1.3% was used for this correction.

5.1.2 Corrections for Radiative Processes

Corrections were made for the radiative processes already mentioned in Section 4.6. The size of the radiative corrections implemented by SIMC is determined by running the full simulation with and without including radiative effects. In each bin, the ratio of the number of events predicted by these two simulations, after the 'standard' cuts of Table 5.3, gives a number equivalent to the correction factor required to take account of the radiative effects. This radiative correction factor is listed for each bin in Table A.1 of the Appendix. These values can be used to remove the effect of the radiative corrections on the cross sections. As illustrated by [50], the uncertainty in the radiative corrections was estimated to be 2%.

5.2 Particle Identification and Event Selection

5.2.1 Coincidence Time and Pion Identification

In this analysis the scattered electron at the SOS and π^+ at the HMS were detected in coincidence. A raw coincidence time was measured by using the trigger of one spectrometer to start a TDC which was stopped by a delayed version of the other spectrometer's trigger. Each single arm pre-trigger was formed according to a 3 out of 4 scintillator planes majority scheme. The raw difference in times between when an electron makes a trigger at the SOS and when a coincident positive particle triggers the HMS,

$$t_{raw} = |t_{electron} - t_{particle}|,$$

were, on an event-by-event basis, corrected for differences in path length of both particles through the spectrometers using measured track information. Corrections on these times were also made for the variation in the velocity β of the positive particle, since all electrons are essentially traveling at the same velocity ($\approx c$). The corrected coincidence time is given by

$$t_c = t_{raw} + corrections \tag{5.4}$$

With the time of flight information of the particles at the HMS, the corrected coincidence time can be adjusted to make a given positive particle appear

at a specific time independent of momentum. By so doing, events of such a particle can be selected by taking a simple interval of the coincidence timing spectrum.

From the reconstructed momentum and energy, a particle's velocity can be calculated such that

$$\beta = \frac{|\mathbf{P}|}{E} = \frac{|\mathbf{P}|}{\sqrt{|\mathbf{P}|^2 + m^2}}, \tag{5.5}$$

where $\mathbf{P}$ and E are in units of c, the speed of light. For a particle type i, the inverse velocity as a function of momentum will be

$$\frac{1}{\beta_i} = \frac{\sqrt{|\mathbf{P}|^2 + m_i^2}}{|\mathbf{P}|}, \tag{5.6}$$

from which we can obtain the time of flight for a given particle by multiplying its inverse velocity by the particle's path length in the HMS, l.

$$t_i(|\mathbf{P}|) = \frac{l}{\beta_i(|\mathbf{P}|)} \tag{5.7}$$

Making the momentum dependence of a desired particle straight will

correspond to a sharper peak for the desired events in a one dimensional coincidence time histogram, see Figure 5.2. Such a histogram allows for accurate selection of the desired events while rejecting the undesired particles. In order to remove the momentum dependence of the pions, the corrected coincidence time was normalized as follows:

$$t_c^{'} = t_c - t_{\pi^+}. \tag{5.8}$$

When such a procedure is employed, the new coincidence time for pions depends only on the actual difference in starting times of the particles in the target, causing the peak of real coincidences to be shifted to zero. Protons and kaons have their coincidence time peaks shifted relative to the pions since for the same momentum, they have different velocities (mass difference). Figure 5.1 shows the much smaller number of detected kaons forming a locus between the protons and pions, and can distinctly be separated as well.

5.2.2 Accidental Corrections

In this experiment, the neutron particles were identified from π^+-e^- coincidences by missing mass reconstruction. So it is essential to neatly select pion events at the HMS which are in coincidence to electrons detected at

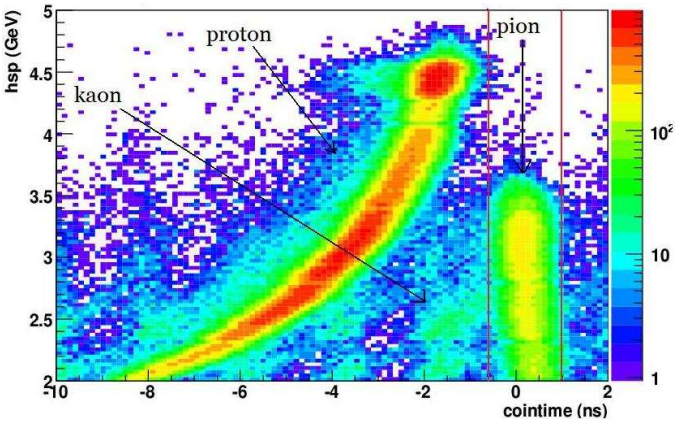

Figure 5.1: $t_c^{'}$ *vs. HMS momentum for coincidence events normalized to make the pion locus vertical. A coincidence time (cointime) cut of* $-0.6 < t_c^{'} < 1.0$ *ns will select the pion events. Note the good separation between pions, protons and kaons.*

the SOS. Coincidence time is the parameter that registers when a pion is detected at the HMS with respect to an electron originating from the same event detected at the SOS.

If within the 100 ns coincidence time window both detectors are triggered by particles originating from different uncorrelated scattering events, then we talk of accidental coincidences.

Within the coincidence time cut of -0.6 ns $< t_c^{'} < 1.0$ ns used to select pion events, the number of accidental coincidences was estimated by determining the average number of accidentals in the left and right flanks of the spectrum free from hadronic contaminants i.e. -50 ns $< t_c^{'} < -10$ ns and 10 ns $< t_c^{'} < 45$ ns respectively. This number was then normalised for the pion coincidence time window of 1.6 ns and subtracted from the data.

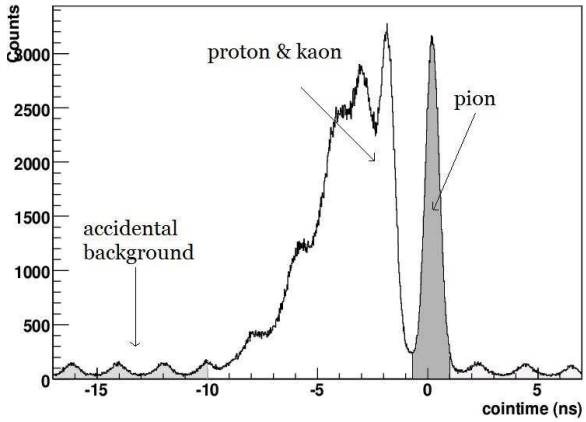

Figure 5.2: *Coincidence time spectrum with dark shaded region representng the 1.6 ns wide pion cut. The 2 ns beam structure is clear in the accidental background flanks.*

5.2.3 Electron Identification

As the π^+ were separated from the protons by using the coincidence time between triggers from both spectrometers, so too were the electrons separated from π^- at the SOS.

Electrons were identified in the SOS using a combination of the SOS gas Čerenkov and the lead glass calorimeter. Electrons which are much lighter than pions had a momentum threshold of 11 MeV as compared to the pion threshold of 2.95 GeV to fire the Čerenkov detector. Since the SOS maximum momentum was below 2.0 GeV, this means that the requirement of a minimum number of Čerenkov photons will enable electrons to be selected over π^-. Figure 5.3 shows electron selection on the portion of the histogram at the right of the cut (arrow). The portion of the data that did not fire the

Čerenkov is evident in the lowest data bin (that is left of the arrow).

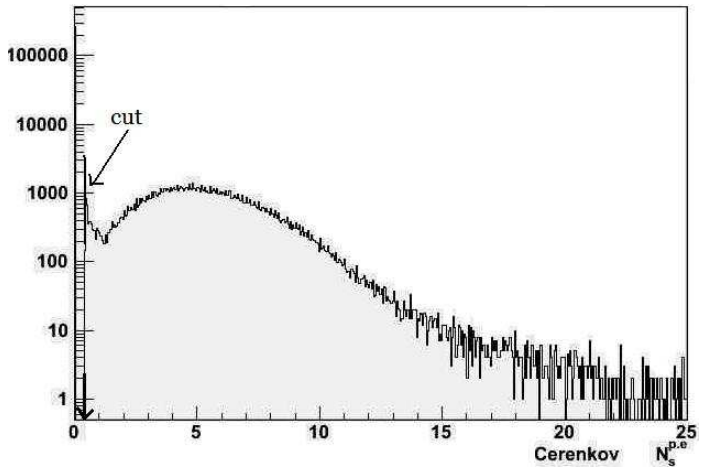

Figure 5.3: *Čerenkov number of photoelectron cut.*

For the lead glass calorimeter, the ratio of the total energy deposited to the measured particle momentum was used to identify electrons. This ratio is expected to be unity for electrons, since an electron's momentum and energy at these highly relativistic energies were practically equal, and an electron deposits all its energy in the calorimeter. The calorimeter signal due to pions was dominated by the creation of Čerenkov light (forming a peak at a ratio of 0.25) with a long tail up to ~ 1 due to the charge exchange nuclear interaction ($\pi^- p \rightarrow \pi^0 n X$) and the subsequent decay, $\pi^0 \rightarrow \gamma\gamma$. The two photons are absorbed in the calorimeter. This peak which is clearly seen in Figure 5.4 also includes other hadronic showers.

Hence the Čerenkov restriction coupled with that of the calorimeter will give an appropriate electron identification at the SOS. The combination of

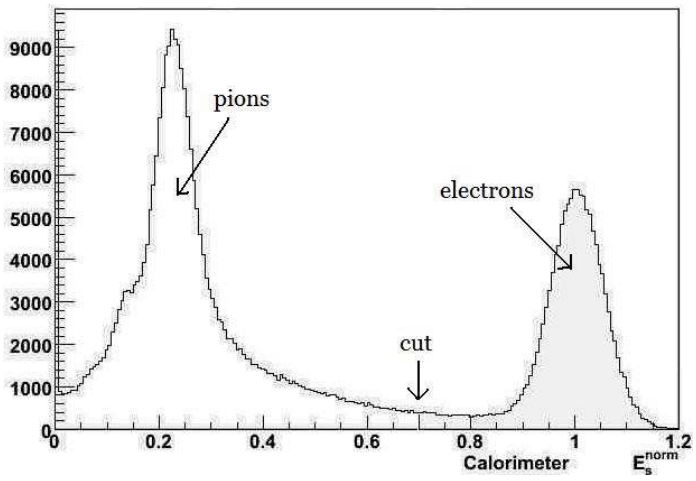

Figure 5.4: *Calorimeter* $E_s^{norm} = \frac{E}{P}$ *plot.*

these two criteria can be graphically evidenced using a two dimensional histogram of the Čerenkov and calorimeter outputs as shown in Figure 5.5.

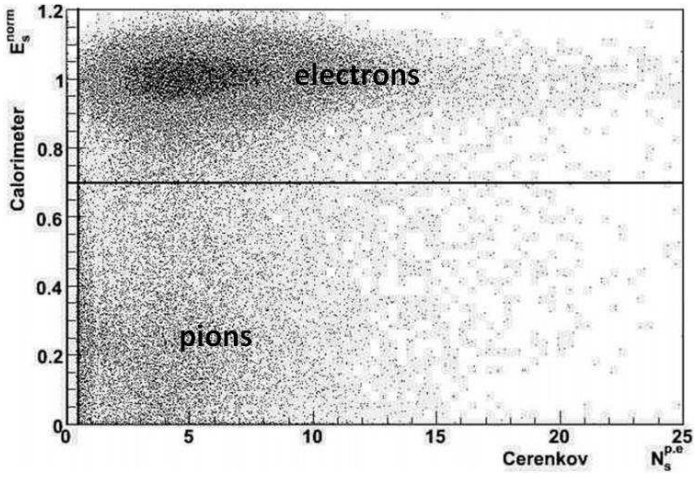

Figure 5.5: *A scatter plot of Čerenkov detector output (number of photo-electron) versus the Calorimeter output (*E_s^{norm}*) showing the combined cuts to select electron events.*

5.2.4 Missing Mass Reconstruction

Because the spectrometer system identified an outgoing electron and a π^+ while we are interested in neutron events (and these events are not directly observed), one must determine the mass of missing neutron by exploiting energy and momentum (4-momentum) conservation as was already discussed in Chapter 1.

For a π^+ detected at the HMS, the general reaction can be written as $p(e, e'\pi^+)X$, where X could only be a neutron from the decay process

$$N^* \rightarrow n + \pi^+ \tag{5.9}$$

or it could also be a nucleon and an extra pion arising from processes like

$$N^* \rightarrow n + \pi^0 + \pi^+, \tag{5.10}$$

or

$$N^* \rightarrow n + \pi^- + \pi^+ + \pi^+ \tag{5.11}$$

The most reliable way to determine the missing particles is to calculate the square of the missing mass which is an invariant. A typical reconstructed missing mass squared spectrum for our process, without any efficiency or background corrections, clearly shows that we are dealing with exclusive

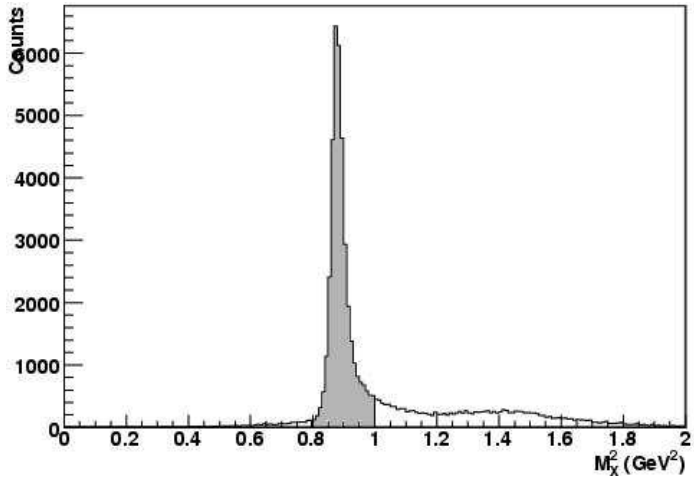

Figure 5.6: $p(e, e'\pi^+)X$ *missing mass squared plot*.

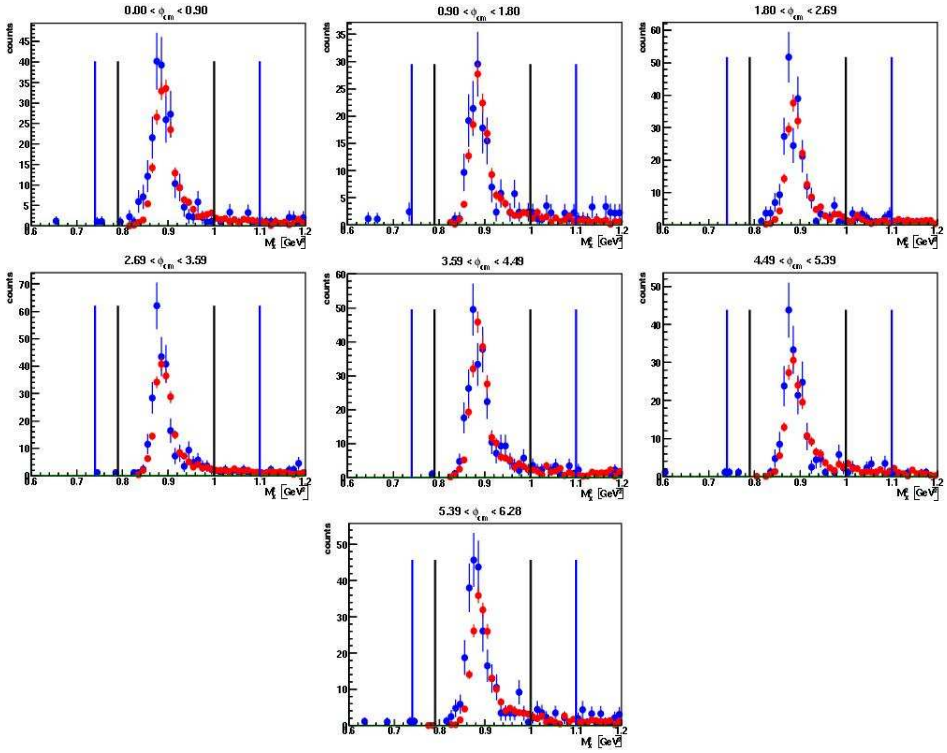

Figure 5.7: *Missing mass squared plots indicating both Monte Carlo simulation (red) and data (blue) and two cuts to select the neutron peak at* 1.68 *GeV* $< W <$ 1.70 *GeV and* $0.9 < \cos\theta_{cm} < 1.0$.

pion production (process 5.9). This is so because we can get the neutron peak at m_n^2 = 0.883 GeV^2 by introducing the cut $0.8 < M_X^2 < 1$. Such a cut does not include the multipion background (arising from process 5.10) which begins at an M_X^2 threshold of $(m_n + m_{\pi^0})^2 = 1.155$ GeV^2 (Figure 5.6). Figure 5.7 shows a very good agreement between the Monte Carlo simulation of the missing mass and our data.

5.3 Data Cuts

The data analysis entailed filtering the raw experimental data and extracting specific relevant events. Extracting the events is not a trivial task, one needed to apply very specific cuts on a number of variables per event that selects only those events with the correct physics for what we are investigating. Only once these cuts are made, and the correct events extracted, can we obtain worthwhile results from the experiment. This process was repeated very many times using different conditions with much discussion on the results, until a satisfactory analysis was achieved.

Table 5.3 consists of the standard cuts applied to the data. Cuts such as the particles momentum deviation at both spectrometers (δ_h and δ_s), are applied to guarantee that use is made only of particles within the well-understood region of the spectrometer momentum acceptance. In addition to the cuts listed in the Table, collimator cuts [51] at both the HMS and SOS

Quantity	Cut	Purpose
electron-pion coincidence time, $t_c^{'}$	$\lvert t_c^{'} - 0.2\rvert < 0.8$ ns	selecting pion
HMS particle momentum deviation, $\delta_h = \frac{P-P_{HMS}}{P_{HMS}}$	$\lvert\delta_h\rvert < 9$ %	HMS acceptance
SOS particle momentum deviation, $\delta_s = \frac{P-P_{SOS}}{P_{SOS}}$	$-17.5\% < \delta_s < 20.0\%$	SOS acceptance
SOS x position focal plane, X_s^{fp}	$-20.0 \leq X_s^{fp} \leq 22.0$	SOS acceptance
SOS shower counter sum, E_s^{norm}	$E_s^{norm} > 0.7$	selecting electron
SOS Čerenkov number of photons, $N_s^{p.e}$	$N_s^{p.e} > 0.5$	selecting electron
Missing mass squared, M_x^2	$0.8 < M_x^2 < 1.0$ GeV^2	selecting neutron

Table 5.3: *Sets of standard cuts applied to the data*.

were used to ensure that the reconstructed track of a detected particle traces back through acceptable regions of the collimator slits.

5.4 Data Distribution

An overview of the acceptance of the detectors is clearly illustrated by the scatter plot of Figure 5.8. The detected pions were very forward going.

Also, the scatter plots of Figure 5.9 show the range of the invariant mass

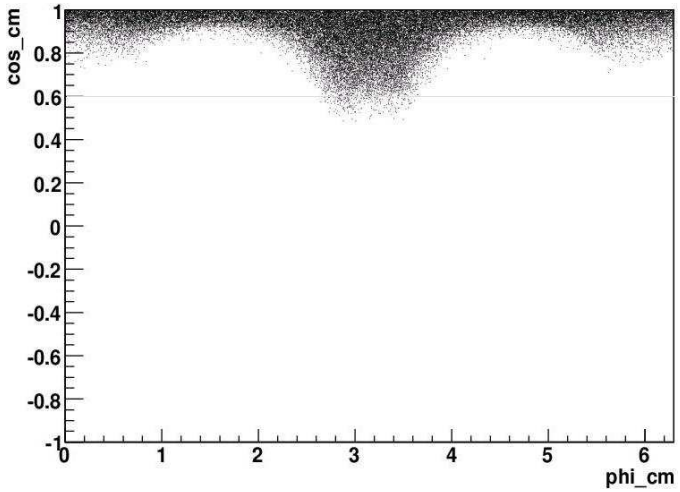

Figure 5.8: *Forward going pions for E01-002, 0.6 $\leq \cos\theta_{cm} \leq$ 1.0. See Figure 1.2 in Section 1.4 to recall the definition of the kinematic variables.*

as well as its Q^2 dependence for the detected pions in this experiment.

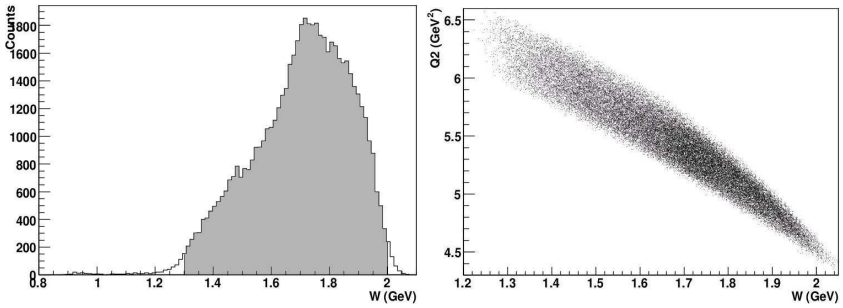

Figure 5.9: *Invariant mass and W versus Q^2 plots for the pion analysis of E01-002.*

For the purpose of extracting the experimental cross section the data were binned in $\{W, \cos\theta_{cm}, \phi_{cm}\}$ as indicated in Table 5.4.

Variable	Range	Bins
W (GeV)	$1.3 \leq W \leq 2.0$	35
$\cos\theta_{cm}$	$0.6 \leq \cos\theta_{cm} \leq 1.0$	4
ϕ_{cm} (rad)	$0 \leq \phi_{cm} \leq 2\pi$	7

Table 5.4: *Pion analysis binning for E01-002.*

5.5 Extracting the Differential Cross Section

In this analysis, the cross section was extracted by using the Monte Carlo ratio method. The normal quantity that can be generated by theory is the differential cross section. In practice, this quantity is measured experimentally but distorted by many systematic and random effects (radiative processes, multiple scattering and other nuclear reactions, acceptance and efficiency issues and so on), and in general, these cannot reliably be deconvoluted from the data. Instead, one subjects a model of the theory to a Monte Carlo procedure simulating the data that model would lead to if it went through the same systematic and random effects as provided by a realistic simulation of the actual experiment (beam, target, spectrometers). This method was implemented in four basic steps:

1. The data yield, Y, was obtained.

2. The Monte Carlo yield, Y_{MC}, determined.

3. The ratio Y/Y_{MC} calculated.

4. The experimental cross section measured was scaled from the ratio.

For each bin in ΔE and $\Delta\Omega$, the number of detected electrons is given by:

$$N^{e^-}_{detected} = L(\frac{d\sigma}{d\Omega dE'})(\Delta E'\Delta\Omega)A(E',\theta)\varepsilon + BG \tag{5.12}$$

where

- $L = N^{e^-}_{beam}N_T$ is the integrated luminosity;
- $N^{e^-}_{beam} = \frac{Q}{e}$ is the number of electrons incident on the target, where Q is the beam charge in Coulombs;
- $N_T = \frac{\rho t N_A}{M}$ is the number of target nuclei per unit area;
- ρ is the target density in gcm^{-3};
- t is the target thickness in cm;
- N_A is Avogadro's number, $6.022 \times 10^{23} mol^{-1}$;
- M is the target mass in atomic mass units (amu);
- ε is the total efficiency for detection;
- $A(E',\theta)$ (the acceptance which is dependent on momentum vector of particle at target and spectrometer optics) reflects the probability that

a particle is transported through the spectrometer to the detectors and the effects from the spectrometer optics are accounted for in the data by simulation in the Monte Carlo spectrometer model and compared with the data; and

- BG are background events.

From Equation (5.12) the efficiency corrected electron yield is

$$Y = \frac{(N^{e^-}_{detected} - BG)}{\varepsilon} = L(\frac{d\sigma}{d\Omega dE'})(\Delta E' \Delta\Omega) A(E', \theta) \tag{5.13}$$

Now, the Monte Carlo data can be simulated using a cross section model to obtain

$$Y_{MC}(E', \theta) = L(\frac{d\sigma}{d\Omega dE'})^{mod}(\Delta E' \Delta\Omega) A_{MC}(E', \theta) \tag{5.14}$$

The Monte Carlo ratio method then consists of taking ratio to data with the assumption that $A_{MC}(E', \theta) = A(E', \theta)$. That is taking ratio of Equations (5.13) and (5.14) we obtain

$$(\frac{d\sigma}{d\Omega dE'})^{data} = (\frac{d\sigma}{d\Omega dE'})^{mod} \frac{Y(E', \theta)}{Y_{MC}(E', \theta)} \tag{5.15}$$

The generated Monte Carlo results were made to be reasonably close to the data such that the same software routines and cuts were used to later analyze both the Monte Carlo results and the data. For each run, the data and Monte Carlo results were binned in W, $cos\theta_{cm}$ and ϕ_{cm}. A missing mass squared (M_x^2) cut containing the missing neutron peak was applied to the data and to the Monte Carlo results, and the results integrated over M_x^2. For each bin, the experimental differential cross section was determined by calculating the ratio of the number of data events to the number of simulated Monte Carlo events and then multiplying this ratio by a model cross section,

$$\sigma^{data} = \sigma^{mod} \frac{N_{data}}{N_{MC}}. \tag{5.16}$$

This follows from Equation (5.15), where N_{data} is the number of pions in the data obtained by multiplying the data yield by the measured experimental charge while N_{MC} is the number of pions generated from SIMC using a model input cross section σ^{mod}. As mentioned in the previous chapter, the Hall C Monte Carlo simulation package (SIMC) includes simulations of a variety of effects such as spectrometer acceptance, radiative corrections, pion decay, multiple scattering and energy loss as well as models for elec-

troproduction cross section.

As our measurement was the highest value of Q^2 measured to date for the reaction $p(e, e'\pi^+)n$, there are not yet simulations in this region, which essentially includes unchartered territory. It was therefore necessary to extrapolate the previously discussed MAID [15] model for pion electroproduction. In this light, the MAID 2003 model of lower Q^2 was weighted by the dipole form factor

$$G = (1 + \frac{Q^2}{0.71})^{-2},$$

and used to extrapolate the pion electroproduction cross section. It should be noted that it is the square of this dipole form factor that contributes to the cross section.

If the input model cross section describes the data well, then the number of experimental and simulated events should be equivalent and their ratio should not show a significant dependence on a particular kinematic variable. However, even if the model rightly describes the kinematic dependence of the data, differences in overall scale cannot be excluded. It is to extract this possible difference in magnitude that the model cross section is weighted by the measured experimental data. The tabulated cross section data are given in Table A.1 at the Appendix.

5.6 Estimates of Uncertainties

Our result can only be meaningful if the statistical uncertainties are correct and the estimates for systematic uncertainties reasonable. The statistical uncertainty on the cross section is determined by the uncertainties in N_{data} and N_{MC} in Equation (5.16). The uncertainty in N_{data} is given by the statistical uncertainty in the number of measured real events and the contributions from accidental coincidence events and events from the cell walls. As the Monte Carlo simulation was done for high statistics, the relative statistical error on $R = N_{data}/N_{MC}$ is dominated by the uncertainty in the number of measured real events.

The procedure used for systematic studies in this work is exactly that applied by Dalton [50] to the $p(e, e'p)\eta$ data. Estimates of systematic uncertainties were accounted for in one of two ways depending on their source. A global uncertainty was assumed and applied to the overall data when such uncertainty was independent of the binned kinematic variables ($W, \cos\theta_{cm}, \phi_{cm}$). Table 5.5 lists various sources of global systematic uncertainty and their estimated sizes. The sizes refer to the percent fraction of measured cross section at all kinematics.

On the other hand, systematic uncertainties that were presumed to be dependent on the kinematic variables were treated on a bin-by-bin basis.

Source	Uncertainty (%)	Reference
SOS acceptance	3.0	Ref. [50]
Radiative Corrections	2.0	Sec. 5.1.2
Trigger efficiency	1.4	Ref. [50]
Pion absorption	1.3	Sec. 5.1.1
HMS acceptance	1.0	Ref. [52]
Target density	0.6	Ref. [1]
Charge measurement	0.5	Ref. [1]
Electron PID cut	0.1	Ref. [1, 51]
Quadrature Sum	4.27	

Table 5.5: *Global systematic uncertainties applied to the data.*

Such uncertainties were estimated by comparing, for each bin, the value of the cross section extracted with a nominal set of variables used in the Monte Carlo simulation to that extracted using adjusted sets of variables. By nominal here, we mean the best set of variables used for the 'standard' analysis from which our final differential cross section was calculated. Each variable (or set of variables) was altered one at a time and the analysis redone up to the stage of obtaining the differential cross section.

Table 5.6 lists various sources of kinematic dependent systematic errors considered in the analysis. Values of these variables were either not exactly known or the determination of the cross section could be sensitive to their changes. For instance, the target position in the beam direction, z_{targ}, was imprecisely known with an uncertainty window of 3 mm. The position of the target defines the entrance angles to the spectrometers, and therefore

Source		Nominal value	Systematic variation	$\langle \delta^{\upsilon} \rangle$ (%)
z_{targ} offset	(mm)	1.5	0.0	3.6
			3.0	3.6
SOS, HMS				
D.C. resolution	(mm)	0.35, 0.57	0.39, 0.63	3.9
M_x^2 cut	(GeV^2)	$0.8 < M_x^2 < 1.0$	$0.7 < M_x^2 < 1.1$	3.7
			$0.84 < M_x^2 < 0.96$	3.3

Table 5.6: *Sources of kinematic dependent systematic errors, values used for the main analysis and their systematic variations, and the weighted mean systematic error for all bins,* $\langle \delta^{\upsilon} \rangle$.

can affect spectrometer quantities. For the standard analysis, an offset of 1.5 mm from the centre was used. The variation chosen for this variable was 1.5 mm on either side of the assumed nominal position. Secondly, the drift chamber resolutions for both spectrometers were altered as indicated in the table. Finally, the dependence of the cross section on the missing mass squared, M_x^2, cut was checked by widening and subsequently tightening the cut over reasonable limits.

The systematic uncertainty in the differential cross section (in the ith bin) resulting from a change in a given variable was considered to be

$$\delta_i^{\upsilon} = \frac{|x_i - y_i^{\upsilon}|}{2},$$

where x_i is the differential cross section obtained from the nominal value of the variable in the main analysis, and y_i^{υ} is the differential cross section obtained from the analysis with the change υ applied to that variable.

In order to appreciate the size of each systematic error in Table 5.5, use is made of $\langle \delta^{\upsilon} \rangle$. This is the mean systematic error for all bins, weighted by the statistical error of the measurement in each bin

$$\langle \delta^{\upsilon} \rangle = \frac{\Sigma_i \delta_i^{\upsilon} / \sigma_i^2}{\Sigma_i 1 / \sigma_i^2},$$

where σ_i is the statistical error of the differential cross section in bin i.

The total systematic uncertainty for the ith bin, δ_i^{tot}, was calculated by adding in quadrature the systematic uncertainty for each variation, δ_i^{υ}, and the global systematic uncertainties, δ_{glo}. That is

$$\delta_i^{tot} = \sqrt{\sum_{\upsilon} (\delta_i^{\upsilon})^2 + \sum \delta_{glo}^2}.$$

Table A.1 at the Appendix tabulates the cross section obtained from nominal values of the variables with separate statistical and estimated systematic errors for each (W, $\cos\theta_{cm}$, ϕ_{cm}) bin.

Chapter 6

Result and Conclusion

In this chapter we shall discuss the result of the analysis and compare it to recent theoretical models. We also compare our measurement to a recent pion electroproduction data. We illustrate the ϕ-dependence of the measured differential cross section and highlight the importance of this data, which is from an extended kinematic region from previous data. We indicate how the data could be used to measure the Q^2 dependence of the transition form factors into higher mass resonances.

6.1 Summary of Results for the Exclusive π^+ Differential Cross Section

Figure 6.1 displays the computed centre-of-mass differential cross sections for the $p(e, e'\pi^+)n$ process done at an average Q^2 of 5.5 GeV^2 at the invariant mass range of 1.3 GeV $\leq$ W $\leq$ 2.0 GeV at the forward angular range of 0.6 $\leq \cos\theta_{cm} \leq$ 1, with full ϕ_{cm} coverage. The cross section was com-

puted in four $\cos\theta_{cm}$ and seven ϕ_{cm} bins. This data set is from an extended kinematic region compared to the most recent studies from CLAS [24] at an average $Q^2 \leq 4.5$ GeV^2 with 1.08 GeV $\leq W \leq$ 1.70 GeV.

With an insignificant background in the missing mass squared plots (Figures 5.6 and 5.7), this analysis is considered to be very clean and two independent parallel analyses with systematic and consistency checks have been done to confirm the results.

Our extracted cross section is about two times stronger than the MAID 2003 model cross section extrapolated to 5.5 GeV^2 using the dipole form factor $G = (1 + \frac{Q^2}{0.71})^{-2}$. Both our cross section and the model peak at more or less the same W but at the most forward angle, $\cos\theta_{cm} > 0.9$, our data grows stronger from $W > 1.8$ GeV. The bumps appear at the second and third resonance regions that consist, amongst other overlapping resonances, of the Roper or $P_{11}(1440)$, the $S_{11}(1535)$ and the $F_{15}(1680)$ resonances.

Figure 6.2 shows a plot of invariant mass versus cross section for the bin centered at $\theta_{cm} = 18^o$ and all seven ϕ_{cm} bins compared to a recent SAID fit [17] and to the CLAS data at the nearest corresponding ϕ_{cm} bins. There is an excellent agreement between the SAID fit and our "BARYON" data for $W > 1.5$ GeV. The same story holds between the recent CLAS data at $Q^2 = 4.2$ GeV^2 with our data for $W < 1.5$ GeV.

Another plot comparing the Q^2 dependence of the CLAS data at $\cos\theta_{cm} =$

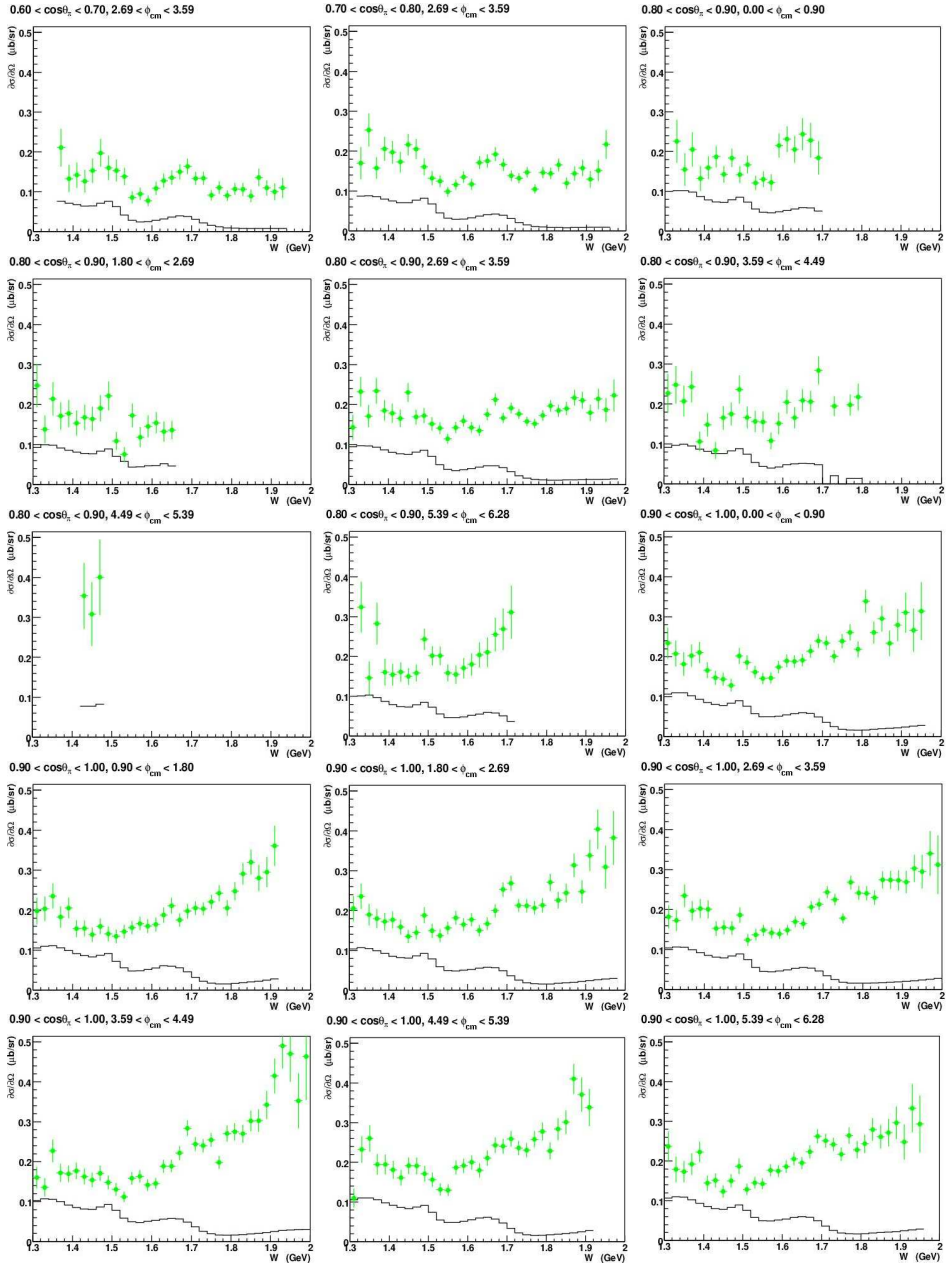

Figure 6.1: *Differential cross section with solid line indicating the MAID 2003 model input cross section.*

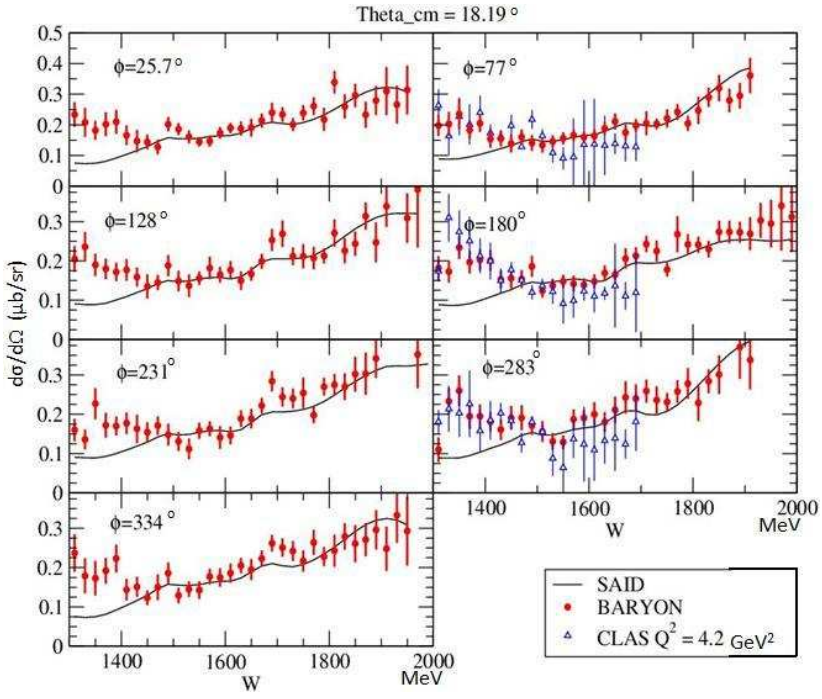

Figure 6.2: *Our "BARYON" data plot of W versus Cross Section at the most forward θ_{cm} bin for all seven ϕ_{cm} bins compared to a recent SAID fit and the CLAS data at $Q^2 = 4.2$ GeV^2.*

1 and $\phi_{cm} = 90^o$ with MAID (Figure 6.3) demonstrates a divergence of the CLAS data from the MAIM at higher W. Two points close to the CLAS $\phi_{cm} = 90^o$ bin from our "BARYON" data were also plotted. An extrapolation by eye to our high Q^2 shows that our data does not follow the expected Q^2 dependence from the lower Q^2 CLAS data or MAID.

The cross section does not have a significant ϕ_{cm} dependence as it is illustrated in the $\partial\sigma/\partial\Omega$ versus ϕ_{cm} plots for some W bins in Figure 6.4.

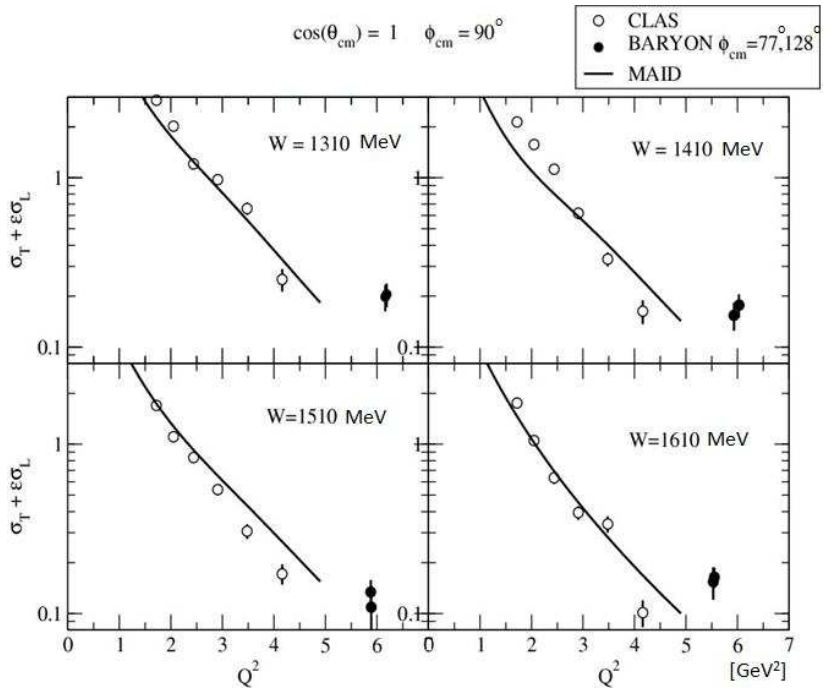

Figure 6.3: *Q^2 dependence of the Cross Section for CLAS data at* $\cos\theta_{cm}$*=1 and* ϕ_{cm}*=90^o with Q^2 dependence for "BARYON" data at same* $\cos\theta_{cm}$ *but two* ϕ_{cm} *bins centered at 77^o and 128^o, since both data were binned differently. Also plotted is the MAID Q^2 dependence which gives a feel for what one would expect if the Q^2 dependence stayed the same above 5 GeV^2. The y-axis is in log scale.*

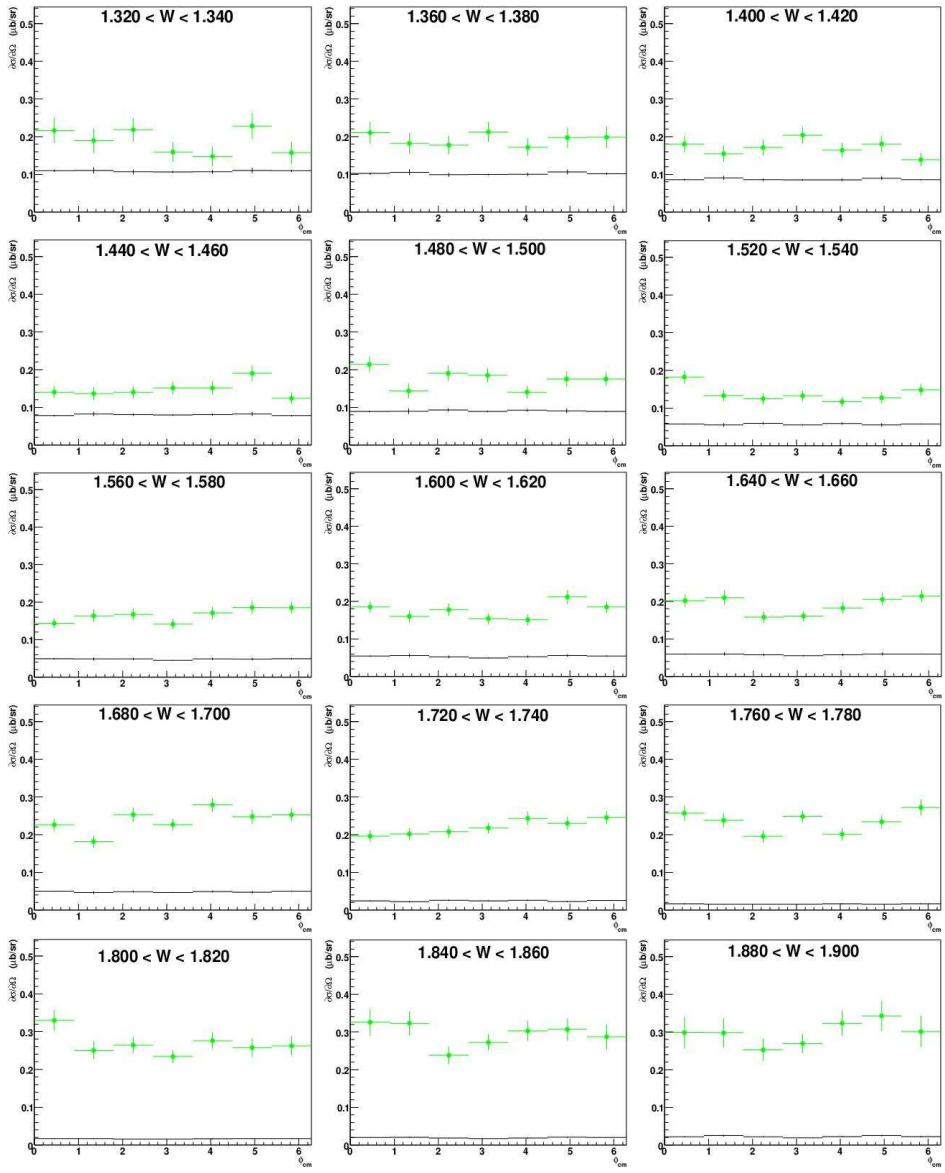

Figure 6.4: *Cross section flat in* ϕ_{cm}.

6.2 Conclusion

We have presented the results of a high statistics measurement of the differential cross section for the process

$$p(e, e'\pi^+)n$$

done at the highest momentum transfer (average Q^2 of 5.5 GeV^2) of this exclusive process to date. The results are sensitive to high-mass baryon resonances and diverge significantly from the MAID 2003 extrapolation (using the square of the dipole form factor $G^2 = (1 + \frac{Q^2}{0.71})^{-4}$) of the lower Q^2 data. Our results suggest that the extrapolation must be more complex than a simple dipole form factor on this theoretical formulation. This might be due to a more correlated interaction between the constituents of the neutron to produce a stronger response of the system than expected by the isobar parameterization of the MAID. Another comparison with a recent SAID fit illustrates the fact that the current state of existing theories does not correlate with these data appropriately. Work with the SAID theoretical group has now begun to use these results, which extend the kinematic range in W and Q^2, for the exclusive π^+ electroproduction process, in order to constrain the large scale theoretical models. The use of our data which is characterized by its very forward angular coverage, together with existing data, could enable the Q^2 dependence of the transition form factors into higher mass reso-

nances to be measured. Such a measurement would improve understanding of the QCD structure of these resonance regions.

Appendix A

A.1 Tabulated Cross Section Data

Table A.1: *Extracted differential cross-section.*

W [GeV]	$\cos\theta_{cm}$	ϕ_{cm} [deg.]	$\langle Q^2_{\rm bin}\rangle$ [$\frac{\rm GeV^2}{\rm c^2}$]	$\langle\epsilon\rangle$	rad. corr.	$\frac{d^2\sigma}{d\Omega_\pi}$ [$\frac{\rm nb}{\rm sr}$]	$\delta_{\rm stat}$ [$\frac{\rm nb}{\rm sr}$]	$\delta_{\rm syst}$ [$\frac{\rm nb}{\rm sr}$]
1.310	0.850	128.6	6.26	0.428	1.08	244.3	53.6	18.1
1.310	0.850	180.0	6.19	0.440	0.94	141.3	31.1	17.6
1.310	0.850	231.4	6.28	0.426	1.02	223.9	47.9	15.2
1.310	0.950	25.7	6.13	0.448	1.08	231.0	38.0	12.1
1.310	0.950	77.1	6.16	0.443	0.98	195.5	33.0	11.4
1.310	0.950	128.6	6.19	0.439	0.97	202.6	31.6	9.6
1.310	0.950	180.0	6.16	0.443	1.04	179.6	28.3	10.1
1.310	0.950	231.4	6.20	0.438	0.99	158.3	27.1	9.3
1.310	0.950	282.9	6.16	0.444	0.92	108.6	23.6	12.1
1.310	0.950	334.3	6.13	0.448	1.00	233.7	37.8	18.7

W	$\cos\theta_{cm}$	ϕ_{cm}	$\langle Q^2_{\rm bin}\rangle$	$\langle\epsilon\rangle$	rad. corr.	$\frac{d^2\sigma}{d\Omega_\pi}$	$\delta_{\rm stat}$	$\delta_{\rm syst}$
[GeV]		[deg.]	$[\frac{\rm GeV^2}{\rm c^2}]$			$[\frac{n\rm b}{\rm sr}]$	$[\frac{n\rm b}{\rm sr}]$	$[\frac{n\rm b}{\rm sr}]$
1.330	0.750	180.0	6.18	0.436	1.00	167.9	39.9	16.9
1.330	0.850	25.7	6.11	0.447	1.24	222.7	53.3	24.0
1.330	0.850	128.6	6.17	0.438	0.97	136.3	34.5	11.2
1.330	0.850	180.0	6.15	0.439	1.04	229.4	36.0	14.0
1.330	0.850	231.4	6.18	0.435	1.18	244.9	46.4	25.1
1.330	0.850	334.3	6.12	0.445	1.17	320.2	62.6	21.1
1.330	0.950	25.7	6.12	0.446	0.96	205.1	32.0	21.6
1.330	0.950	77.1	6.12	0.447	1.01	200.7	30.2	16.6
1.330	0.950	128.6	6.17	0.437	1.10	232.8	31.6	13.5
1.330	0.950	180.0	6.14	0.442	1.10	170.8	26.0	8.3
1.330	0.950	231.4	6.16	0.438	1.00	133.9	22.9	8.8
1.330	0.950	282.9	6.11	0.447	1.07	229.7	32.9	11.4
1.330	0.950	334.3	6.12	0.446	1.25	177.1	32.0	15.8
1.350	0.750	180.0	6.12	0.439	1.00	250.1	40.8	12.5
1.350	0.850	25.7	6.08	0.445	1.13	152.9	40.6	19.4
1.350	0.850	128.6	6.16	0.434	1.01	211.6	40.9	14.3
1.350	0.850	180.0	6.12	0.438	0.99	169.0	27.7	9.3
1.350	0.850	231.4	6.16	0.436	0.97	204.7	38.2	15.0
1.350	0.850	334.3	6.08	0.445	1.35	144.0	41.2	12.9

W [GeV]	$\cos\theta_{cm}$	ϕ_{cm} [deg.]	$\langle Q^2_{\rm bin}\rangle$ [$\frac{\rm GeV^2}{\rm c^2}$]	$\langle\epsilon\rangle$	rad. corr.	$\frac{d^2\sigma}{d\Omega_\pi}$ [$\frac{n\rm b}{\rm sr}$]	$\delta_{\rm stat}$ [$\frac{n\rm b}{\rm sr}$]	$\delta_{\rm syst}$ [$\frac{n\rm b}{\rm sr}$]
1.350	0.950	25.7	6.09	0.444	1.12	179.4	29.2	8.3
1.350	0.950	77.1	6.07	0.448	0.90	232.3	30.7	23.9
1.350	0.950	128.6	6.15	0.434	0.97	187.5	26.2	9.2
1.350	0.950	180.0	6.11	0.440	1.00	231.5	28.0	10.7
1.350	0.950	231.4	6.15	0.436	1.00	224.2	27.8	19.2
1.350	0.950	282.9	6.08	0.447	0.97	257.0	33.0	14.7
1.350	0.950	334.3	6.09	0.444	0.97	170.8	26.4	20.9
1.370	0.650	180.0	6.13	0.429	1.05	207.9	46.7	12.8
1.370	0.750	180.0	6.08	0.437	0.87	155.7	27.3	14.6
1.370	0.850	25.7	6.05	0.444	1.09	202.5	43.0	24.6
1.370	0.850	128.6	6.14	0.428	1.01	169.2	34.0	14.9
1.370	0.850	180.0	6.08	0.438	1.02	231.0	31.6	20.1
1.370	0.850	231.4	6.10	0.433	1.02	239.9	38.7	23.2
1.370	0.850	334.3	6.04	0.444	1.22	279.1	51.8	16.1
1.370	0.950	25.7	6.08	0.438	1.04	199.9	27.6	17.2
1.370	0.950	77.1	6.01	0.449	0.96	180.7	26.1	9.4
1.370	0.950	128.6	6.13	0.431	0.98	177.4	23.9	9.5
1.370	0.950	180.0	6.09	0.436	1.00	194.6	24.2	12.8
1.370	0.950	231.4	6.12	0.433	0.98	170.1	22.4	14.6

W	$\cos\theta_{cm}$	ϕ_{cm}	$\langle Q^2_{\rm bin}\rangle$	$\langle\epsilon\rangle$	rad. corr.	$\frac{d^2\sigma}{d\Omega_\pi}$	$\delta_{\rm stat}$	$\delta_{\rm syst}$
[GeV]		[deg.]	$[\frac{\rm GeV^2}{\rm c^2}]$			$[\frac{n\rm b}{\rm sr}]$	$[\frac{n\rm b}{\rm sr}]$	$[\frac{n\rm b}{\rm sr}]$
1.370	0.950	282.9	6.02	0.448	0.98	192.5	25.9	13.8
1.370	0.950	334.3	6.08	0.438	1.03	189.8	26.7	12.8
1.390	0.650	180.0	6.10	0.428	1.08	131.3	34.1	9.7
1.390	0.750	180.0	6.05	0.435	0.97	203.1	29.9	17.2
1.390	0.850	25.7	6.06	0.434	0.96	130.5	31.4	13.9
1.390	0.850	128.6	6.10	0.430	0.99	175.2	33.9	9.4
1.390	0.850	180.0	6.05	0.434	1.00	182.9	25.7	9.7
1.390	0.850	231.4	6.08	0.431	0.91	104.8	24.2	9.6
1.390	0.850	334.3	6.06	0.434	1.05	158.6	33.1	17.9
1.390	0.950	25.7	6.04	0.436	1.13	207.8	26.3	15.1
1.390	0.950	77.1	5.97	0.448	0.92	202.8	25.3	11.5
1.390	0.950	128.6	6.07	0.432	0.98	170.1	21.8	8.0
1.390	0.950	180.0	6.05	0.434	1.04	200.0	23.3	10.5
1.390	0.950	231.4	6.08	0.430	0.99	167.6	20.6	10.3
1.390	0.950	282.9	5.97	0.448	1.03	192.4	24.4	11.2
1.390	0.950	334.3	6.04	0.437	1.01	220.1	25.3	16.0
1.410	0.650	180.0	6.05	0.426	0.97	140.0	31.4	7.0
1.410	0.750	180.0	6.00	0.434	1.07	194.7	28.2	12.4
1.410	0.850	25.7	6.03	0.431	0.99	157.5	28.2	9.2

W [GeV]	$\cos\theta_{cm}$	ϕ_{cm} [deg.]	$\langle Q^2_{\rm bin}\rangle$ [$\frac{\rm GeV^2}{\rm c^2}$]	$\langle\epsilon\rangle$	rad. corr.	$\frac{d^2\sigma}{d\Omega_\pi}$ [$\frac{n\rm b}{\rm sr}$]	$\delta_{\rm stat}$ [$\frac{n\rm b}{\rm sr}$]	$\delta_{\rm syst}$ [$\frac{n\rm b}{\rm sr}$]
1.410	0.850	128.6	6.05	0.430	0.99	151.7	31.1	9.6
1.410	0.850	180.0	6.01	0.432	0.99	175.8	23.7	15.0
1.410	0.850	231.4	6.01	0.434	1.03	146.6	28.9	10.4
1.410	0.850	334.3	6.02	0.431	1.01	152.0	27.1	11.9
1.410	0.950	25.7	6.01	0.434	0.96	164.0	19.8	16.6
1.410	0.950	77.1	5.93	0.447	0.98	151.9	20.9	12.2
1.410	0.950	128.6	6.03	0.431	1.06	174.4	21.2	10.2
1.410	0.950	180.0	6.02	0.432	1.01	198.0	22.1	12.2
1.410	0.950	231.4	6.03	0.431	1.00	174.9	20.4	10.2
1.410	0.950	282.9	5.92	0.447	0.98	178.7	21.9	9.5
1.410	0.950	334.3	6.01	0.434	0.96	142.6	19.0	11.1
1.430	0.650	180.0	6.02	0.423	0.97	125.1	28.2	9.8
1.430	0.750	180.0	5.98	0.431	1.07	170.7	25.4	10.8
1.430	0.850	25.7	5.97	0.432	1.02	184.6	26.5	12.7
1.430	0.850	128.6	5.97	0.430	1.06	165.9	31.4	9.9
1.430	0.850	180.0	5.97	0.431	1.04	163.4	21.8	11.9
1.430	0.850	231.4	5.99	0.428	1.04	82.8	20.9	6.2
1.430	0.850	282.9	5.98	0.430	1.07	349.7	81.4	37.7
1.430	0.850	334.3	5.97	0.432	1.02	158.7	24.3	13.2

W	$\cos\theta_{cm}$	ϕ_{cm}	$\langle Q^2_{\rm bin}\rangle$	$\langle\epsilon\rangle$	rad. corr.	$\frac{d^2\sigma}{d\Omega_\pi}$	$\delta_{\rm stat}$	$\delta_{\rm syst}$
[GeV]		[deg.]	$[\frac{\rm GeV^2}{\rm c^2}]$			$[\frac{n\rm b}{\rm sr}]$	$[\frac{n\rm b}{\rm sr}]$	$[\frac{n\rm b}{\rm sr}]$
1.430	0.950	25.7	5.97	0.433	0.94	145.3	17.2	19.1
1.430	0.950	77.1	5.89	0.445	0.96	152.6	19.7	12.2
1.430	0.950	128.6	5.96	0.433	1.01	156.6	18.9	10.8
1.430	0.950	180.0	5.97	0.431	1.12	150.9	18.0	8.6
1.430	0.950	231.4	5.97	0.432	1.07	161.0	19.2	15.4
1.430	0.950	282.9	5.90	0.444	1.04	159.3	19.7	11.2
1.430	0.950	334.3	5.97	0.432	0.97	149.1	17.5	12.5
1.450	0.650	180.0	5.99	0.421	0.98	151.1	30.4	12.0
1.450	0.750	180.0	5.94	0.428	1.02	213.5	26.5	10.3
1.450	0.850	25.7	5.92	0.432	0.94	140.8	20.7	9.2
1.450	0.850	128.6	5.92	0.432	1.06	162.0	30.3	10.8
1.450	0.850	180.0	5.93	0.429	0.96	227.2	23.4	13.6
1.450	0.850	231.4	5.93	0.432	1.10	163.3	29.0	11.8
1.450	0.850	282.9	5.91	0.436	1.12	304.0	79.0	53.0
1.450	0.850	334.3	5.92	0.432	1.03	147.7	20.8	8.2
1.450	0.950	25.7	5.94	0.430	1.07	141.9	16.6	10.2
1.450	0.950	77.1	5.88	0.439	1.01	137.0	17.9	13.7
1.450	0.950	128.6	5.91	0.433	0.99	133.5	16.3	15.4
1.450	0.950	180.0	5.94	0.429	1.09	153.7	17.2	11.4

W [GeV]	$\cos\theta_{cm}$	ϕ_{cm} [deg.]	$\langle Q^2_{\rm bin}\rangle$ [$\frac{\rm GeV^2}{\rm c^2}$]	$\langle\epsilon\rangle$	rad. corr.	$\frac{d^2\sigma}{d\Omega_\pi}$ [$\frac{n\rm b}{\rm sr}$]	$\delta_{\rm stat}$ [$\frac{n\rm b}{\rm sr}$]	$\delta_{\rm syst}$ [$\frac{n\rm b}{\rm sr}$]
1.450	0.950	231.4	5.92	0.432	1.12	152.5	17.9	11.0
1.450	0.950	282.9	5.87	0.441	1.06	188.9	20.7	14.0
1.450	0.950	334.3	5.93	0.430	0.97	121.8	15.1	8.8
1.470	0.650	180.0	5.94	0.420	1.05	194.9	34.5	15.0
1.470	0.750	180.0	5.90	0.426	0.96	202.7	24.9	10.1
1.470	0.850	25.7	5.88	0.431	0.98	181.4	22.9	21.1
1.470	0.850	128.6	5.86	0.435	1.00	188.4	32.5	10.4
1.470	0.850	180.0	5.88	0.428	0.91	166.6	18.5	17.1
1.470	0.850	231.4	5.86	0.429	0.92	172.4	28.1	15.5
1.470	0.850	282.9	5.87	0.434	1.04	395.3	93.4	57.4
1.470	0.850	334.3	5.88	0.431	0.97	156.5	20.5	10.9
1.470	0.950	25.7	5.89	0.428	1.07	126.6	15.6	11.1
1.470	0.950	77.1	5.86	0.433	1.01	157.5	19.1	11.5
1.470	0.950	128.6	5.85	0.434	1.00	143.0	16.8	7.3
1.470	0.950	180.0	5.89	0.428	0.97	151.8	17.0	9.8
1.470	0.950	231.4	5.86	0.434	1.08	169.0	18.8	9.7
1.470	0.950	282.9	5.84	0.436	1.05	188.5	21.1	13.3
1.470	0.950	334.3	5.89	0.428	1.02	148.2	16.7	16.0
1.490	0.650	180.0	5.91	0.415	0.98	158.1	30.0	13.9

W [GeV]	$\cos\theta_{cm}$	ϕ_{cm} [deg.]	$\langle Q^2_{\rm bin}\rangle$ [$\frac{\rm GeV^2}{\rm c^2}$]	$\langle\epsilon\rangle$	rad. corr.	$\frac{d^2\sigma}{d\Omega_\pi}$ [$\frac{n\rm b}{\rm sr}$]	$\delta_{\rm stat}$ [$\frac{n\rm b}{\rm sr}$]	$\delta_{\rm syst}$ [$\frac{n\rm b}{\rm sr}$]
1.490	0.750	180.0	5.85	0.424	0.99	158.4	20.9	12.5
1.490	0.850	25.7	5.83	0.430	0.99	140.5	20.7	11.5
1.490	0.850	128.6	5.81	0.435	1.11	218.6	35.5	14.3
1.490	0.850	180.0	5.84	0.427	0.92	170.2	18.9	13.2
1.490	0.850	231.4	5.87	0.427	1.05	233.4	35.0	13.9
1.490	0.850	334.3	5.83	0.429	1.03	240.0	26.6	12.8
1.490	0.950	25.7	5.84	0.427	0.96	199.3	19.5	12.0
1.490	0.950	77.1	5.84	0.426	0.99	139.0	18.4	12.0
1.490	0.950	128.6	5.81	0.433	0.97	185.7	19.8	13.6
1.490	0.950	180.0	5.85	0.426	1.10	183.8	19.1	11.0
1.490	0.950	231.4	5.80	0.435	0.99	146.2	17.3	11.2
1.490	0.950	282.9	5.84	0.428	1.02	169.0	19.7	9.2
1.490	0.950	334.3	5.85	0.428	0.96	184.1	18.9	12.0
1.510	0.650	180.0	5.87	0.414	1.03	151.3	27.3	14.5
1.510	0.750	180.0	5.81	0.424	0.99	130.5	17.4	9.8
1.510	0.850	25.7	5.79	0.429	0.97	164.9	21.8	11.0
1.510	0.850	128.6	5.89	0.416	0.99	107.4	22.0	16.3
1.510	0.850	180.0	5.80	0.426	1.01	149.7	16.4	8.6
1.510	0.850	231.4	5.76	0.433	0.94	164.3	26.7	31.4

W	$\cos\theta_{cm}$	ϕ_{cm}	$\langle Q^2_{\rm bin}\rangle$	$\langle\epsilon\rangle$	rad. corr.	$\frac{d^2\sigma}{d\Omega_\pi}$	$\delta_{\rm stat}$	$\delta_{\rm syst}$
[GeV]		[deg.]	$[\frac{\rm GeV^2}{\rm c^2}]$			$[\frac{n\rm b}{\rm sr}]$	$[\frac{n\rm b}{\rm sr}]$	$[\frac{n\rm b}{\rm sr}]$
1.510	0.850	334.3	5.79	0.429	0.99	199.3	24.1	10.1
1.510	0.950	25.7	5.82	0.424	1.03	183.6	17.8	9.2
1.510	0.950	77.1	5.88	0.413	0.99	132.7	16.9	9.6
1.510	0.950	128.6	5.76	0.433	1.00	147.3	17.3	13.3
1.510	0.950	180.0	5.81	0.425	1.10	122.3	15.1	7.1
1.510	0.950	231.4	5.76	0.433	0.99	129.2	15.6	11.5
1.510	0.950	282.9	5.86	0.418	0.95	154.3	17.9	11.8
1.510	0.950	334.3	5.81	0.425	0.96	127.0	14.5	9.4
1.530	0.650	180.0	5.81	0.414	0.97	136.6	21.6	10.7
1.530	0.750	180.0	5.76	0.422	0.96	122.9	14.5	10.4
1.530	0.850	25.7	5.75	0.426	0.99	119.5	17.8	11.1
1.530	0.850	128.6	5.71	0.433	0.94	74.4	18.7	7.3
1.530	0.850	180.0	5.75	0.424	0.99	139.2	14.7	7.3
1.530	0.850	231.4	5.76	0.421	1.09	154.5	26.2	12.7
1.530	0.850	334.3	5.74	0.429	0.96	199.0	22.9	15.2
1.530	0.950	25.7	5.77	0.422	0.99	159.3	15.3	11.4
1.530	0.950	77.1	5.82	0.413	1.06	144.5	16.6	7.3
1.530	0.950	128.6	5.73	0.429	1.08	135.1	15.9	12.9
1.530	0.950	180.0	5.77	0.421	1.07	135.1	14.3	7.5

W [GeV]	$\cos\theta_{cm}$	ϕ_{cm} [deg.]	$\langle Q^2_{\rm bin}\rangle$ [$\frac{\rm GeV^2}{\rm c^2}$]	$\langle\epsilon\rangle$	rad. corr.	$\frac{d^2\sigma}{d\Omega_\pi}$ [$\frac{n\rm b}{\rm sr}$]	$\delta_{\rm stat}$ [$\frac{n\rm b}{\rm sr}$]	$\delta_{\rm syst}$ [$\frac{n\rm b}{\rm sr}$]
1.530	0.950	231.4	5.74	0.428	0.97	110.8	13.2	14.0
1.530	0.950	282.9	5.82	0.413	1.02	129.7	15.2	9.1
1.530	0.950	334.3	5.77	0.422	1.04	143.4	14.5	8.9
1.550	0.650	180.0	5.78	0.411	0.99	84.6	15.0	8.3
1.550	0.750	180.0	5.72	0.421	0.92	97.2	12.0	6.0
1.550	0.850	25.7	5.69	0.427	0.93	128.5	19.5	11.3
1.550	0.850	128.6	5.79	0.416	1.17	170.7	29.3	15.7
1.550	0.850	180.0	5.72	0.421	0.87	113.2	12.3	8.7
1.550	0.850	231.4	5.72	0.426	0.97	153.2	25.3	9.2
1.550	0.850	334.3	5.70	0.426	0.96	156.6	21.0	9.1
1.550	0.950	25.7	5.73	0.420	0.99	143.4	14.0	7.5
1.550	0.950	77.1	5.77	0.416	1.02	154.3	16.4	8.2
1.550	0.950	128.6	5.68	0.427	0.97	154.1	15.7	7.3
1.550	0.950	180.0	5.73	0.419	1.03	146.4	14.0	8.4
1.550	0.950	231.4	5.68	0.427	1.10	156.4	15.6	10.1
1.550	0.950	282.9	5.73	0.418	1.05	127.8	14.7	6.9
1.550	0.950	334.3	5.73	0.420	1.02	141.1	13.6	10.9
1.570	0.650	180.0	5.72	0.412	0.99	93.1	15.3	7.8
1.570	0.750	180.0	5.68	0.418	0.97	114.6	13.0	7.0

W [GeV]	$\cos\theta_{cm}$	ϕ_{cm} [deg.]	$\langle Q^2_{\rm bin}\rangle$ [$\frac{\rm GeV^2}{\rm c^2}$]	$\langle\epsilon\rangle$	rad. corr.	$\frac{d^2\sigma}{d\Omega_\pi}$ [$\frac{n\rm b}{\rm sr}$]	$\delta_{\rm stat}$ [$\frac{n\rm b}{\rm sr}$]	$\delta_{\rm syst}$ [$\frac{n\rm b}{\rm sr}$]
1.570	0.850	25.7	5.66	0.424	0.95	120.7	20.6	9.6
1.570	0.850	128.6	5.59	0.430	1.01	116.9	24.9	12.1
1.570	0.850	180.0	5.68	0.418	0.92	140.8	14.0	7.8
1.570	0.850	231.4	5.74	0.407	0.97	106.4	20.5	9.1
1.570	0.850	334.3	5.65	0.424	1.02	152.5	23.0	10.7
1.570	0.950	25.7	5.68	0.418	1.01	145.0	13.9	9.3
1.570	0.950	77.1	5.68	0.418	1.04	164.3	17.0	8.9
1.570	0.950	128.6	5.66	0.423	0.96	179.3	17.3	12.7
1.570	0.950	180.0	5.68	0.418	1.05	140.1	13.7	9.6
1.570	0.950	231.4	5.65	0.424	1.03	161.3	15.4	8.9
1.570	0.950	282.9	5.66	0.421	1.01	184.6	17.6	12.7
1.570	0.950	334.3	5.68	0.419	0.97	174.4	14.8	11.2
1.590	0.650	180.0	5.68	0.408	0.96	76.8	13.4	4.9
1.590	0.750	180.0	5.64	0.415	0.87	133.7	14.1	8.7
1.590	0.850	25.7	5.62	0.420	1.02	212.4	30.1	11.9
1.590	0.850	128.6	5.51	0.428	0.97	143.6	27.7	8.2
1.590	0.850	180.0	5.64	0.415	0.96	157.4	14.7	12.1
1.590	0.850	231.4	5.65	0.417	1.19	149.6	27.0	18.6
1.590	0.850	334.3	5.61	0.422	1.04	168.5	25.2	15.2

W	$\cos\theta_{cm}$	ϕ_{cm}	$\langle Q^2_{\rm bin}\rangle$	$\langle\epsilon\rangle$	rad. corr.	$\frac{d^2\sigma}{d\Omega_\pi}$	$\delta_{\rm stat}$	$\delta_{\rm syst}$
[GeV]		[deg.]	$[\frac{\rm GeV^2}{\rm c^2}]$			$[\frac{n\rm b}{\rm sr}]$	$[\frac{n\rm b}{\rm sr}]$	$[\frac{n\rm b}{\rm sr}]$
1.590	0.950	25.7	5.65	0.415	1.03	171.7	15.1	10.3
1.590	0.950	77.1	5.62	0.421	1.07	158.2	17.2	7.4
1.590	0.950	128.6	5.61	0.420	1.02	163.2	15.9	10.6
1.590	0.950	180.0	5.63	0.417	1.04	137.6	13.0	6.9
1.590	0.950	231.4	5.60	0.423	1.03	139.7	14.3	15.1
1.590	0.950	282.9	5.61	0.423	1.03	189.0	18.1	8.9
1.590	0.950	334.3	5.64	0.416	1.01	172.4	14.7	12.3
1.610	0.650	180.0	5.63	0.409	1.03	107.1	16.4	6.2
1.610	0.750	180.0	5.59	0.414	0.99	115.7	13.8	5.4
1.610	0.850	25.7	5.56	0.420	0.97	228.1	32.2	14.9
1.610	0.850	128.6	5.53	0.419	1.03	152.4	26.2	12.1
1.610	0.850	180.0	5.60	0.413	1.01	140.9	13.7	6.2
1.610	0.850	231.4	5.55	0.419	0.91	202.3	29.3	12.9
1.610	0.850	334.3	5.55	0.421	0.96	177.7	27.9	18.2
1.610	0.950	25.7	5.60	0.413	1.03	187.3	15.5	9.1
1.610	0.950	77.1	5.55	0.423	1.13	162.2	17.5	9.3
1.610	0.950	128.6	5.60	0.413	1.03	175.2	15.9	11.3
1.610	0.950	180.0	5.58	0.415	1.02	146.6	12.9	9.1
1.610	0.950	231.4	5.58	0.417	0.98	143.9	14.0	12.5

W	$\cos\theta_{cm}$	ϕ_{cm}	$\langle Q^2_{\rm bin}\rangle$	$\langle\epsilon\rangle$	rad. corr.	$\frac{d^2\sigma}{d\Omega_\pi}$	$\delta_{\rm stat}$	$\delta_{\rm syst}$
[GeV]		[deg.]	$[\frac{\rm GeV^2}{\rm c^2}]$			$[\frac{n\rm b}{\rm sr}]$	$[\frac{n\rm b}{\rm sr}]$	$[\frac{n\rm b}{\rm sr}]$
1.610	0.950	282.9	5.55	0.423	1.06	197.5	18.0	16.7
1.610	0.950	334.3	5.60	0.414	1.11	183.7	15.3	10.5
1.630	0.650	180.0	5.58	0.406	1.07	126.4	17.4	6.4
1.630	0.750	180.0	5.55	0.411	0.93	169.1	16.3	10.7
1.630	0.850	25.7	5.51	0.418	0.99	202.9	33.1	14.4
1.630	0.850	128.6	5.49	0.414	0.86	130.6	24.4	15.3
1.630	0.850	180.0	5.55	0.411	1.01	133.5	12.9	8.1
1.630	0.850	231.4	5.54	0.414	0.99	163.5	26.2	11.3
1.630	0.850	334.3	5.50	0.420	0.96	201.1	31.3	14.3
1.630	0.950	25.7	5.56	0.412	1.02	186.0	15.2	12.0
1.630	0.950	77.1	5.48	0.424	1.05	185.2	18.5	8.9
1.630	0.950	128.6	5.57	0.410	1.01	148.3	14.3	13.1
1.630	0.950	180.0	5.54	0.413	1.03	167.3	13.6	8.9
1.630	0.950	231.4	5.55	0.414	1.03	186.2	16.3	9.9
1.630	0.950	282.9	5.49	0.423	1.13	177.5	17.7	11.7
1.630	0.950	334.3	5.55	0.412	1.00	202.7	15.8	11.0
1.650	0.650	180.0	5.54	0.404	0.99	133.7	17.3	9.8
1.650	0.750	180.0	5.51	0.408	0.96	173.3	16.5	8.4
1.650	0.850	25.7	5.45	0.419	1.05	240.7	39.8	15.0

W	$\cos\theta_{cm}$	ϕ_{cm}	$\langle Q^2_{\rm bin}\rangle$	$\langle\epsilon\rangle$	rad. corr.	$\frac{d^2\sigma}{d\Omega_\pi}$	$\delta_{\rm stat}$	$\delta_{\rm syst}$
[GeV]		[deg.]	$[\frac{\rm GeV^2}{\rm c^2}]$			$[\frac{n\rm b}{\rm sr}]$	$[\frac{n\rm b}{\rm sr}]$	$[\frac{n\rm b}{\rm sr}]$
1.650	0.850	128.6	5.58	0.379	0.86	134.5	22.5	13.5
1.650	0.850	180.0	5.50	0.410	0.98	173.2	14.2	7.9
1.650	0.850	231.4	5.54	0.406	1.06	206.3	27.8	10.1
1.650	0.850	334.3	5.44	0.421	0.96	207.6	36.7	16.2
1.650	0.950	25.7	5.51	0.409	1.01	189.1	15.3	16.9
1.650	0.950	77.1	5.49	0.411	1.05	208.3	19.1	11.7
1.650	0.950	128.6	5.52	0.408	1.04	164.9	15.5	7.8
1.650	0.950	180.0	5.49	0.412	1.02	162.4	13.3	7.9
1.650	0.950	231.4	5.50	0.410	0.99	186.6	15.7	13.4
1.650	0.950	282.9	5.46	0.418	1.04	208.0	18.9	18.1
1.650	0.950	334.3	5.51	0.410	0.99	192.7	15.2	15.7
1.670	0.650	180.0	5.48	0.403	1.02	147.9	18.5	7.7
1.670	0.750	180.0	5.47	0.404	0.98	190.1	17.2	8.8
1.670	0.850	25.7	5.40	0.418	1.05	225.3	43.2	16.7
1.670	0.850	180.0	5.46	0.407	1.02	209.5	15.3	10.6
1.670	0.850	231.4	5.51	0.402	0.96	203.4	26.6	26.8
1.670	0.850	334.3	5.40	0.418	0.84	251.7	42.1	25.3
1.670	0.950	25.7	5.47	0.407	1.02	211.5	16.3	12.8
1.670	0.950	77.1	5.49	0.402	1.03	173.2	16.6	13.7

W	$\cos\theta_{cm}$	ϕ_{cm}	$\langle Q^2_{\rm bin}\rangle$	$\langle\epsilon\rangle$	rad. corr.	$\frac{d^2\sigma}{d\Omega_\pi}$	$\delta_{\rm stat}$	$\delta_{\rm syst}$
[GeV]		[deg.]	$[\frac{\rm GeV^2}{\rm c^2}]$			$[\frac{n\rm b}{\rm sr}]$	$[\frac{n\rm b}{\rm sr}]$	$[\frac{n\rm b}{\rm sr}]$
1.670	0.950	128.6	5.46	0.408	1.02	196.9	16.3	10.6
1.670	0.950	180.0	5.45	0.410	1.00	203.8	14.3	15.4
1.670	0.950	231.4	5.44	0.411	0.99	218.8	17.4	10.3
1.670	0.950	282.9	5.47	0.407	0.97	240.3	19.3	22.9
1.670	0.950	334.3	5.46	0.408	1.06	220.6	16.6	12.9
1.690	0.650	180.0	5.44	0.401	0.95	161.9	19.2	8.8
1.690	0.750	180.0	5.42	0.404	0.92	163.8	15.4	11.2
1.690	0.850	25.7	5.36	0.416	0.93	181.9	41.4	25.7
1.690	0.850	180.0	5.41	0.405	0.98	164.3	12.9	9.7
1.690	0.850	231.4	5.38	0.416	1.09	280.6	34.3	19.8
1.690	0.850	334.3	5.35	0.417	1.19	265.2	51.6	26.9
1.690	0.950	25.7	5.42	0.405	1.10	236.6	17.5	15.1
1.690	0.950	77.1	5.52	0.391	1.11	195.1	17.8	10.1
1.690	0.950	128.6	5.40	0.409	0.95	249.6	18.2	15.4
1.690	0.950	180.0	5.40	0.408	0.98	210.6	14.3	13.3
1.690	0.950	231.4	5.40	0.410	1.02	280.3	19.4	13.7
1.690	0.950	282.9	5.46	0.400	0.98	237.3	18.6	20.5
1.690	0.950	334.3	5.40	0.408	1.04	258.8	17.9	12.6
1.710	0.650	180.0	5.38	0.401	0.92	131.9	16.4	13.5

W	$\cos\theta_{cm}$	ϕ_{cm}	$\langle Q^2_{\rm bin}\rangle$	$\langle\epsilon\rangle$	rad. corr.	$\frac{d^2\sigma}{d\Omega_\pi}$	$\delta_{\rm stat}$	$\delta_{\rm syst}$
[GeV]		[deg.]	$[\frac{\rm GeV^2}{\rm c^2}]$			$[\frac{n\rm b}{\rm sr}]$	$[\frac{n\rm b}{\rm sr}]$	$[\frac{n\rm b}{\rm sr}]$
1.710	0.750	180.0	5.38	0.402	0.94	136.5	13.7	9.1
1.710	0.850	180.0	5.36	0.405	1.00	188.9	13.3	9.2
1.710	0.850	334.3	5.30	0.416	1.23	307.0	66.3	37.8
1.710	0.950	25.7	5.36	0.406	1.06	231.3	16.9	12.3
1.710	0.950	77.1	5.48	0.385	1.03	202.6	16.8	21.7
1.710	0.950	128.6	5.33	0.410	1.01	265.4	18.7	17.3
1.710	0.950	180.0	5.36	0.405	0.98	240.4	14.8	14.4
1.710	0.950	231.4	5.33	0.411	1.02	241.2	17.6	11.9
1.710	0.950	282.9	5.46	0.390	1.17	256.1	19.5	15.7
1.710	0.950	334.3	5.36	0.406	1.01	247.9	17.1	13.6
1.730	0.650	180.0	5.33	0.399	0.96	132.1	16.4	7.2
1.730	0.750	180.0	5.32	0.401	0.99	130.5	12.8	7.9
1.730	0.850	180.0	5.32	0.402	1.04	174.0	12.2	10.3
1.730	0.850	231.4	5.37	0.407	1.08	192.3	24.5	15.6
1.730	0.950	25.7	5.31	0.404	1.01	198.6	15.5	10.9
1.730	0.950	77.1	5.44	0.380	0.97	200.8	16.3	9.4
1.730	0.950	128.6	5.29	0.406	1.01	209.8	16.0	11.4
1.730	0.950	180.0	5.31	0.404	0.98	221.9	13.9	14.7
1.730	0.950	231.4	5.27	0.410	0.98	236.9	16.6	14.8

W	$\cos\theta_{cm}$	ϕ_{cm}	$\langle Q^2_{\rm bin}\rangle$	$\langle\epsilon\rangle$	rad. corr.	$\frac{d^2\sigma}{d\Omega_\pi}$	$\delta_{\rm stat}$	$\delta_{\rm syst}$
[GeV]		[deg.]	$[\frac{\rm GeV^2}{\rm c^2}]$			$[\frac{n\rm b}{\rm sr}]$	$[\frac{n\rm b}{\rm sr}]$	$[\frac{n\rm b}{\rm sr}]$
1.730	0.950	282.9	5.41	0.384	1.08	233.1	17.5	15.9
1.730	0.950	334.3	5.30	0.405	0.98	238.8	16.5	14.0
1.750	0.650	180.0	5.28	0.398	1.00	90.3	13.1	8.9
1.750	0.750	180.0	5.26	0.400	0.97	145.3	13.0	11.1
1.750	0.850	180.0	5.26	0.402	0.98	155.8	11.5	9.2
1.750	0.950	25.7	5.24	0.403	1.01	235.9	17.6	14.3
1.750	0.950	77.1	5.36	0.384	1.01	218.2	17.2	14.8
1.750	0.950	128.6	5.28	0.398	1.08	209.3	16.2	14.5
1.750	0.950	180.0	5.25	0.404	0.97	176.0	12.2	11.3
1.750	0.950	231.4	5.24	0.405	0.97	251.1	17.2	23.3
1.750	0.950	282.9	5.35	0.386	1.06	227.9	17.7	12.0
1.750	0.950	334.3	5.24	0.405	1.09	214.5	17.0	13.3
1.770	0.650	180.0	5.22	0.396	1.05	109.1	15.3	6.7
1.770	0.750	180.0	5.21	0.399	1.03	103.8	11.3	6.7
1.770	0.850	180.0	5.21	0.400	1.03	150.6	11.7	8.8
1.770	0.850	231.4	5.28	0.396	0.91	195.1	26.1	25.9
1.770	0.950	25.7	5.19	0.403	1.04	257.3	20.2	13.6
1.770	0.950	77.1	5.29	0.386	1.00	239.3	19.9	13.3
1.770	0.950	128.6	5.27	0.391	1.01	204.0	16.8	13.3

W	$\cos\theta_{cm}$	ϕ_{cm}	$\langle Q^2_{\rm bin}\rangle$	$\langle\epsilon\rangle$	rad. corr.	$\frac{d^2\sigma}{d\Omega_\pi}$	$\delta_{\rm stat}$	$\delta_{\rm syst}$
[GeV]		[deg.]	$[\frac{\rm GeV^2}{\rm c^2}]$			$[\frac{n\rm b}{\rm sr}]$	$[\frac{n\rm b}{\rm sr}]$	$[\frac{n\rm b}{\rm sr}]$
1.770	0.950	180.0	5.19	0.402	1.07	264.6	16.6	21.5
1.770	0.950	231.4	5.22	0.399	1.08	195.8	15.9	11.8
1.770	0.950	282.9	5.28	0.388	1.07	254.9	20.3	12.9
1.770	0.950	334.3	5.18	0.405	1.01	261.1	20.2	16.3
1.790	0.650	180.0	5.16	0.396	0.91	89.2	13.3	7.4
1.790	0.750	180.0	5.16	0.398	1.05	144.5	14.1	12.0
1.790	0.850	180.0	5.15	0.399	1.03	170.8	13.3	11.6
1.790	0.850	231.4	5.14	0.398	1.05	214.8	33.2	18.3
1.790	0.950	25.7	5.14	0.401	0.96	215.6	19.9	20.2
1.790	0.950	77.1	5.20	0.390	0.97	202.6	19.5	11.5
1.790	0.950	128.6	5.23	0.386	0.96	210.4	17.5	10.6
1.790	0.950	180.0	5.14	0.400	1.04	238.5	16.7	13.1
1.790	0.950	231.4	5.19	0.392	1.02	267.0	20.1	13.2
1.790	0.950	282.9	5.19	0.392	1.00	274.3	22.5	18.3
1.790	0.950	334.3	5.12	0.404	1.01	225.5	20.9	11.3
1.810	0.650	180.0	5.11	0.395	0.94	105.5	14.9	11.0
1.810	0.750	180.0	5.09	0.397	1.03	142.3	14.5	7.9
1.810	0.850	180.0	5.09	0.397	1.01	194.3	14.5	11.2
1.810	0.950	25.7	5.08	0.401	1.04	334.7	28.1	20.3

W	$\cos\theta_{cm}$	ϕ_{cm}	$\langle Q^2_{\rm bin}\rangle$	$\langle\epsilon\rangle$	rad. corr.	$\frac{d^2\sigma}{d\Omega_\pi}$	$\delta_{\rm stat}$	$\delta_{\rm syst}$
[GeV]		[deg.]	$[\frac{\rm GeV^2}{\rm c^2}]$			$[\frac{n\rm b}{\rm sr}]$	$[\frac{n\rm b}{\rm sr}]$	$[\frac{n\rm b}{\rm sr}]$
1.810	0.950	77.1	5.11	0.394	0.96	244.2	22.7	23.9
1.810	0.950	128.6	5.19	0.382	1.06	267.2	21.5	15.9
1.810	0.950	180.0	5.09	0.398	0.97	237.6	17.3	11.6
1.810	0.950	231.4	5.15	0.388	1.01	271.5	21.1	14.8
1.810	0.950	282.9	5.11	0.394	0.98	225.8	21.1	24.9
1.810	0.950	334.3	5.07	0.403	0.94	240.4	23.1	21.1
1.830	0.650	180.0	5.05	0.394	1.03	104.6	16.2	6.4
1.830	0.750	180.0	5.04	0.395	0.97	163.3	16.2	7.9
1.830	0.850	180.0	5.03	0.397	0.95	182.6	15.0	13.1
1.830	0.950	25.7	5.02	0.399	0.96	257.1	27.4	19.2
1.830	0.950	77.1	5.03	0.396	0.95	286.8	26.9	14.9
1.830	0.950	128.6	5.12	0.383	0.99	222.9	20.5	15.7
1.830	0.950	180.0	5.04	0.397	0.97	227.1	17.9	11.9
1.830	0.950	231.4	5.09	0.387	1.00	266.6	22.0	19.6
1.830	0.950	282.9	5.03	0.398	1.03	280.1	27.0	15.3
1.830	0.950	334.3	5.01	0.402	0.99	275.7	27.7	16.4
1.850	0.650	180.0	4.99	0.394	0.96	88.3	15.6	6.5
1.850	0.750	180.0	4.98	0.395	0.96	118.2	14.8	6.9
1.850	0.850	180.0	4.97	0.396	1.00	187.9	16.3	9.1

W	$\cos\theta_{cm}$	ϕ_{cm}	$\langle Q^2_{\rm bin}\rangle$	$\langle\epsilon\rangle$	rad. corr.	$\frac{d^2\sigma}{d\Omega_\pi}$	$\delta_{\rm stat}$	$\delta_{\rm syst}$
[GeV]		[deg.]	$[\frac{\rm GeV^2}{\rm c^2}]$			$[\frac{n\rm b}{\rm sr}]$	$[\frac{n\rm b}{\rm sr}]$	$[\frac{n\rm b}{\rm sr}]$
1.850	0.950	25.7	4.96	0.398	1.00	291.9	31.8	16.0
1.850	0.950	77.1	4.95	0.399	1.02	315.9	30.8	19.3
1.850	0.950	128.6	5.04	0.385	0.99	241.4	23.3	13.0
1.850	0.950	180.0	4.98	0.396	1.01	270.9	21.0	13.6
1.850	0.950	231.4	5.03	0.388	1.01	298.6	25.9	24.3
1.850	0.950	282.9	4.95	0.401	0.96	297.5	29.3	24.6
1.850	0.950	334.3	4.95	0.401	1.00	257.7	29.5	22.8
1.870	0.650	180.0	4.92	0.394	1.07	134.4	21.5	11.3
1.870	0.750	180.0	4.92	0.395	0.96	142.3	17.8	11.6
1.870	0.850	180.0	4.91	0.395	1.00	214.3	19.2	10.8
1.870	0.950	25.7	4.91	0.397	0.94	230.5	31.6	18.8
1.870	0.950	77.1	4.87	0.403	1.03	276.9	32.4	14.5
1.870	0.950	128.6	4.96	0.388	1.05	309.6	29.1	16.8
1.870	0.950	180.0	4.92	0.395	0.98	270.6	22.6	14.9
1.870	0.950	231.4	4.95	0.390	0.97	299.2	27.6	28.1
1.870	0.950	282.9	4.87	0.403	1.01	405.1	37.8	28.4
1.870	0.950	334.3	4.89	0.399	0.99	268.1	34.3	18.5
1.890	0.650	180.0	4.86	0.393	0.90	108.1	19.4	12.6
1.890	0.750	180.0	4.86	0.394	0.98	155.8	20.0	9.1

W	$\cos\theta_{cm}$	ϕ_{cm}	$\langle Q^2_{\rm bin}\rangle$	$\langle\epsilon\rangle$	rad. corr.	$\frac{d^2\sigma}{d\Omega_\pi}$	$\delta_{\rm stat}$	$\delta_{\rm syst}$
[GeV]		[deg.]	$[\frac{\rm GeV^2}{\rm c^2}]$			$[\frac{n\rm b}{\rm sr}]$	$[\frac{n\rm b}{\rm sr}]$	$[\frac{n\rm b}{\rm sr}]$
1.890	0.850	180.0	4.85	0.394	0.98	207.8	20.9	10.6
1.890	0.950	25.7	4.85	0.395	0.98	275.7	39.6	19.1
1.890	0.950	77.1	4.78	0.407	0.97	291.5	37.5	15.7
1.890	0.950	128.6	4.87	0.391	0.99	244.2	28.8	24.3
1.890	0.950	180.0	4.86	0.394	1.01	269.4	24.6	13.0
1.890	0.950	231.4	4.86	0.394	1.04	338.0	34.6	21.7
1.890	0.950	282.9	4.79	0.406	1.09	366.0	43.0	35.8
1.890	0.950	334.3	4.84	0.398	0.98	292.6	40.4	22.1
1.910	0.650	180.0	4.80	0.392	0.98	98.9	21.1	6.5
1.910	0.750	180.0	4.80	0.392	1.01	127.8	20.5	8.8
1.910	0.850	180.0	4.79	0.393	0.92	177.0	20.6	23.2
1.910	0.950	25.7	4.80	0.393	0.99	306.4	49.3	32.6
1.910	0.950	77.1	4.72	0.409	1.13	356.1	49.7	18.8
1.910	0.950	128.6	4.79	0.393	1.00	334.3	38.5	25.0
1.910	0.950	180.0	4.79	0.393	1.10	265.7	27.7	20.4
1.910	0.950	231.4	4.77	0.397	0.88	410.0	42.9	28.8
1.910	0.950	282.9	4.72	0.408	0.89	333.9	46.0	35.0
1.910	0.950	334.3	4.78	0.396	0.97	244.6	43.5	22.0
1.930	0.650	180.0	4.74	0.392	1.03	108.4	24.9	7.2

W	$\cos\theta_{cm}$	ϕ_{cm}	$\langle Q^2_{\rm bin}\rangle$	$\langle\epsilon\rangle$	rad. corr.	$\frac{d^2\sigma}{d\Omega_\pi}$	$\delta_{\rm stat}$	$\delta_{\rm syst}$
[GeV]		[deg.]	$[\frac{\rm GeV^2}{\rm c^2}]$			$[\frac{n\rm b}{\rm sr}]$	$[\frac{n\rm b}{\rm sr}]$	$[\frac{n\rm b}{\rm sr}]$
1.930	0.750	180.0	4.74	0.392	1.10	149.3	25.6	12.4
1.930	0.850	180.0	4.73	0.393	0.88	211.2	25.7	27.3
1.930	0.950	25.7	4.73	0.393	1.01	262.9	53.0	21.5
1.930	0.950	128.6	4.73	0.393	0.90	399.2	48.9	34.0
1.930	0.950	180.0	4.73	0.393	0.98	299.2	33.7	21.2
1.930	0.950	231.4	4.72	0.397	0.96	483.6	55.5	39.9
1.930	0.950	334.3	4.72	0.394	0.97	328.9	60.3	22.9
1.950	0.750	180.0	4.67	0.393	1.04	214.1	35.7	13.9
1.950	0.850	180.0	4.68	0.392	0.93	184.5	29.2	17.2
1.950	0.950	25.7	4.67	0.392	0.99	310.0	71.7	23.3
1.950	0.950	128.6	4.68	0.392	1.04	305.6	53.3	18.5
1.950	0.950	180.0	4.67	0.392	1.07	291.2	41.7	23.9
1.950	0.950	231.4	4.67	0.395	1.35	464.3	69.4	58.9
1.950	0.950	334.3	4.67	0.394	1.07	289.8	70.5	27.6
1.970	0.850	180.0	4.61	0.392	0.87	220.0	39.5	21.5
1.970	0.950	128.6	4.63	0.390	0.80	377.6	66.8	69.8
1.970	0.950	180.0	4.61	0.392	1.00	336.0	55.2	52.3
1.970	0.950	231.4	4.60	0.394	1.01	347.8	68.3	31.7
1.990	0.950	180.0	4.56	0.391	1.14	308.0	72.6	26.7

W	$\cos\theta_{cm}$	ϕ_{cm}	$\langle Q^2_{\rm bin}\rangle$	$\langle\epsilon\rangle$	$\frac{\text{rad.}}{\text{corr.}}$	$\frac{d^2\sigma}{d\Omega_\pi}$	$\delta_{\rm stat}$	$\delta_{\rm syst}$
[GeV]		[deg.]	$[\frac{\rm GeV^2}{\rm c^2}]$			$[\frac{n\rm b}{\rm sr}]$	$[\frac{n\rm b}{\rm sr}]$	$[\frac{n\rm b}{\rm sr}]$
1.990	0.950	231.4	4.54	0.394	1.18	457.4	107.8	74.3

References

[1] T. Horn. PhD thesis, University of Maryland, 2006.

[2] R. Hofstadter. *Rev. Mod. Phys*, 28:214, 1956.

[3] J. I. Friedman and H. W. Kendall. *Ann. Rev. Nucl. Sci*, 22:203, 1972.

[4] C. S. Amstrong. PhD thesis, College of Williams and Mary, 1998.

[5] P. J. Mulders. *Phys. Rep*, 185:83, 1990.

[6] David Griffiths. *Introduction to Elementary Particles*. WILEY, 1987.

[7] F. Halzen and A. D. Martin. *QUARKS AND LEPTONS: An Introductory Course in Modern Particle Physics*. JOHN WILEY and SONS, 1983.

[8] N. Isgur. *Nuclear physics from the quark model with chromodynamics*. Acta Austriaca, 1985.

[9] M. Warns. A relativized quark model for radiative baryon transitions. *Z. Phys. C*, 45:613, 1990.

[10] I. G. Aznauryan. Relativistic effects, QCD mixing angles and N $\rightarrow$ Nγ and $\Delta \rightarrow$ Nγ transition form factors. *Z. Phys. A*, 346:297, 1993.

[11] F. E. Close and Z. P. Lee. Photoproduction and Electroproduction of N^* in a Quark Model with QCD. *Phys. Rev. D*, 42:2194, 1990.

[12] V. Christov. Baryons as non-topological chiral solitons. *Prog. Part. Nucl. Phys.*, 37:91, 1996.

[13] R. L. Walker. Phenomenological Analysis of Single Pion Photoproduction. *Phys. Rev.*, 182:1729, 1969.

[14] V. D. Burkert and L. Elouadrhiri. E_{1+}/M_{1+} and S_{1+}/M_{1+} from an Analysis of $p(e, e'p)\pi^0$ in the Region of the $\Delta(1232)$ Resonance at Q^2 = 3.2 GeV^2. *Phys. Rev. Lett.*, 75:3614, 1995.

[15] D. Drechsel, O. Hanstein, S. S. Kamalov, and L. Tiator. A unitary isobar model for pion photo- and electroproduction on the proton up to 1 GeV. *Nucl. Phys. A*, 645:145, 1999.

[16] R.A. Arndt *et al. Phys. Rev.*, C52:2120, 1995.

[17] R.A. Arndt *et al. Phys. Rev.*, 53:430, 1996.

[18] R.A. Arndt *et al. Phys. Rev.*, A18:449–455, 2003.

[19] N. Isgur and J. Parton. Flux-tube model for hadrons in QCD. *Phys. Rev. D*, 31:2910, 1985.

[20] E. Evangelides. Electroproduction of π^+ mesons in the second and third resonance regions. *Nucl. Phys. B*, 71:381, 1974.

[21] H. Breuker. Forward π^+ electroproduction in the first resonance region at four momentum transfers q^2 = -0.15 and -0.3 GeV^2. *Nucl. Phys. B*, 146:285, 1978.

[22] H. Breuker. Electroproduction of π^+ Mesons at forward and backward directions in the region of D_{13}(1520) and F_{15}(1688) Resonances.

[23] E. Havanes. PhD thesis, College of William and Mary, 2001.

[24] P. Kijun. PhD thesis, Kyungpook National University, 2005.

[25] G. Krafft and A. Hofler. How the Linac Beam Position Monitors Work. Technical report, CEBAF, 1993.

[26] P. Gueye. Status of the Actual Beam Position Monitors in the Hall C Beamline. Technical report, Jefferson Lab Hall C. unpublished.

[27] C. Yan, R. Carlini, and D. Neuffer. Beam Energy Measurement Using the Arc Beam Line as a Spectrometer. Technical report, CEBAF-PR-93-004, 1993.

[28] L. H. Harwood. Technical report, CEBAF-PR-89-006, 1989.

[29] Orbit shift: Analysis and modeling of BSY-ARC transport line optics

in absolute beam energy measurement at Hall C. Technical report, Jlab-TN-99-066, 1999.

[30] Hall C beam momentum measurement system. Technical report, CEBAF-TN-92-054, 1993. unpublished.

[31] J. Dunne. Cryo and dummy target information. Technical report, TJNAF Hall C document, 1998. unpublished.

[32] D. Meekins. Dissertation. College of William and Mary, 1998. unpublished.

[33] B. Terburg. Dissertation. University of Illinois, 1998. unpublished.

[34] D. J. Gaskell. PhD thesis, Oregon State University, 2001.

[35] M. Knott. *Nuc. Inst. and Meth.*, A352:486, 1994.

[36] W. R. Leo. *Tecniques for Nuclear and Particle Physics Experiments*. Springer-Verlag, 1994.

[37] R. Asaturyan. *Nucl. Instrum. Meth.*, A548:364–374, 2005.

[38] D. Abbott. *Proceedings of the IEEE Conference on Real-time Computer Applications in Nuclear, Particle, and Plasma Physics*. Michigan state University - NSCL, East Lansing, 1995.

[39] J. Volmer. PhD thesis, Vrije Universiteit, 2000.

[40] K. Makino and M. Berz. *Nucl. Instrum. Meth.*, A427:338, 1999.

[41] C. Caso *et al*. Review of Particle Physics. *Eur. Phys.*, J. C3:1–794, 1998.

[42] L. Alvarez-Gaume. *Phys. Lett*, B592:1, 2004.

[43] J. Volmer. Calculation of Energy Losses in Hall C's Replay Engine. Technical report, Jefferson Lab Hall C.

[44] L. M. Mo and Y. S. Tsai. *Rev. Mod. Phys*, 41:205, 1969.

[45] Y. S. Tsai. *Phys. Rev*, 122:122, 1961.

[46] N. C. R. Makins. PhD thesis, Massachussetts Institute of Technology, 1994.

[47] R. Ent. *Phys. Rev*, C64, 2001.

[48] T. G. O'Neill. PhD thesis, California Institute of Technology, 1994.

[49] D.F. Geesaman and S. Wood. Hall C Analysis Software Vade Mecum. Jlab Hall C Internal Report, 1994.

[50] M.M. Dalton *et al*. http://arxiv.org/abs/0804.3509. 2008.

[51] A. N. Villano. PhD thesis, Rensselaer Polytechnic Institute, 2007.

[52] F. Renard *et al.* (GRAAL). *Phys. Lett.*, B528:215, 2002. hep-ex/0011098.